

Iron and zinc isotopes reveal redox reactions associated with fluid flow in subduction zones

Skylar F. Beadle Goliber

A thesis

submitted to the Faculty of

the department of Earth and Environmental Sciences

in partial fulfillment

of the requirements for the degree of

Master of Science

Boston College
Morrissey College of Arts and Sciences
Graduate School

November 2022

Abstract

Subduction zones are areas of significant mass transfer between Earth's crust and mantle. The dehydration of water-rich minerals such as serpentinite and lawsonite introduces water and volatiles into the subduction interface, that then travel to the mantle wedge above. The chemical composition, speciation, and redox effect of these fluids carry important implications for arc volcanism and the mobility of economically significant elements. This study uses Fe and Zn isotopic variation in eclogite-breccias from the Monviso ophiolite, combined with Sm-Nd garnet geochronology, to study the composition and redox effects of fluids that were produced during eclogite and blueschist facies metamorphism, and the timescales over which the brecciation and fluid flux events happened. Fe and Zn isotopic measurements were made on a series of four breccia matrix generations (M1-M4), generated during the progressive brecciation of the original Fe-Ti gabbros and the influx of both internally and externally derived fluids. The $\delta^{56}\text{Fe}$ and $\delta^{66}\text{Zn}$ data display a bi-modal distribution, with early matrix crystallization (M1-3) imparting progressively lighter $\delta^{66}\text{Zn}$ values while the $\delta^{56}\text{Fe}$ remains relatively unchanged. The last stage of metasomatic rind formation (M4) is associated with a decrease in both Fe and Zn isotopic values and a particularly significant shift in the Fe isotopes. This distribution suggests that early brecciation (M1-3) resulted from small-scale internal fluid flow that did not have a measurable effect on the isotopic composition and redox state of the system. By contrast, late metasomatic rind formation (M4) was facilitated by the flow of large amounts of external fluids with a strongly negative Fe and Zn isotope signature that affected the redox state of the mafic slab and

may be responsible for transferring oxidized material into the mantle wedge. Dating of the M4 matrix generation yielded an age of 41.31 ± 0.60 Ma. A compilation of age data from Monviso suggests peak metamorphism and initial brecciation (M1 formation) likely occurred at ~ 45 Ma, the formation of the M4 matrix representing the end of eclogite-facies retrogression and brecciation at ~ 41 Ma, and final blueschist and greenschist retrogression at $\sim 38-35$ Ma, yielding timescale of ~ 4 Ma for the entire history of brecciation and fluid flux associated with the Monviso eclogite breccias.

TABLE OF CONTENTS

Title.....	i
Table of Contents.....	v
List of tables.....	vi
List of figures.....	vii
Acknowledgements.....	viii
Chapter 1.....	1
Chapter 2.....	3
1. Introduction.....	3
2. Background and Geologic Setting	7
2.1 Redox Conditions at Convergent Boundaries.....	7
2.2 The Monviso Ophiolite: A Rock Record of Fluid Movement.....	10
3. Sample Descriptions.....	15
4. Methods.....	15
4.1 Microprobe Analysis	17
4.2 Iron and Zinc Isotope	17
4.3 Sm-Nd Garnet Geochronology	19
5. Results.....	21
5.1 Microprobe Results.....	21
5.2 Iron and Zinc Isotope Results.....	22
5.3 Sm-Nd Garnet Geochronology Results.....	24
6. Discussion.....	26
6.1 Isotopic Composition of Fluids in the Monviso Ophiolite	27
6.2 Fluid Sources and Implications for Redox Processes	32
6.3 Timescales of Fluid and Deformation Processes	35
7. Conclusions.....	38
References	39
Supplementary Materials	48

List of Tables

Table 1	14
Table 2	20

List of Figures

Figure 1	4
Figure 2	7
Figure 3	12
Figure 4	19
Figure 5	21
Figure 6	23
Figure 7	26
Figure 8	34

ACKNOWLEDGEMENTS

I would like to thank my fellow lab mates, Charlotte Lorthioir, Dylan Seal, Kyra Croft, Ben Alexander, Kasey Corrado, Ben Shultz, Tassilo Sajonia, Kayleigh Harvey, and Paul Starr. Thank you to Stephanie Walker for your unwavering patience and mentorship, and for talking books with me over the TIMS. Charlotte, starting graduate school during quarantine would not have been possible without you. Special thanks to Paul Starr for his continued support, advice, and for being an unmatched source of petrology knowledge. Thank you to Ethan Baxter, my advisor, for always standing behind me and having faith in me. I would also like to thank Mark Behn for his thoughtful comments on this thesis and for his excellent direction of the graduate studies program – Mark and Ethan’s support of all the graduate students during the hybrid semesters of 2020 and 2021 will never be forgotten. Thank you to my committee members throughout my time at Boston College: Alan Kafta, Seth Kruckenburg, and Jeremy Shakun.

I would like to thank my collaborators Philippe Agard, Edward Inglis, and Frédéric Moynier for their limitless scientific knowledge and for hosting me in Paris. Special thanks to Clément Herviou, Kevin Mendes, Thomas Gyomlai, and Guillaume Bonnet for helping me feel welcome at ISTeP, for showing me the wonders of Rue Mouffetard, and for teaching me how to take a real lunch break. Finally, I would like to thank Cam for sticking with me through the good and the bad, and my parents for listening to me go on about isotope geochemistry and supporting me throughout my education.

Chapter 1

PREFACE TO THE THESIS

The following contains the written thesis for the degree of Master of Sciences in Geological Sciences, awarded to Skylar Goliber, the author of this manuscript. This work began in September of 2020 at Boston College and ended in August of 2022. This thesis was advised by Dr. Ethan Baxter and Dr. Paul Starr. The radiometric dating portion of the following work was completed at the Boston College Center for Isotope Geochemistry with the assistance of Dr. Stephanie Walker and Dr. Kayleigh Harvey. The geological interpretations and stable isotope analysis took place in Paris, France at IStEP, Sorbonne Université with the assistance of Dr. Philippe Agard and at the Institut de Physique du Globe de Paris (IPGP) with the assistance of Dr. Edward Inglis and Dr. Frédéric Moynier. Chapter 2 of this thesis will be submitted for publication at Earth and Planetary Science Letters in the near future.

This document contains an extensive literature review of the formation of the Alpine Mountains, theoretical implications of the oxidation of the upper mantle, why the redox state of the subducting slab is important, but difficult, to study, and the reasoning behind utilizing iron, zinc, and samarium-neodymium isotopes to study these processes. This literature review can be found in the Introduction and Background sections. Also included are the methods used to separate and measure iron and zinc isotopes, as well as the Sm-Nd radiometric dating techniques used at the BC CIG between 2020 and 2022. These techniques are well-equipped to analyze incredibly small amounts of Nd, decreasing the amount of rock material needed to produce accurate and precise isochrons. After describing the methods of data collection and the results, I will discuss the possible implications of these data and the space for future work that pertains to this project.

The reported Sm-Nd bulk garnet ages are the first to be successfully completed for the Lago Superiore Unit in the Monviso Ophiolite. The age of 41.31 ± 0.60 Ma corresponds to the garnet crystallization associated with retrograde metasomatism that eclogite-facies blocks experienced during exhumation. The combination of iron and zinc isotopes compared across distinct matrix generations is novel, and display information regarding the source, composition, and movement mechanism of subduction-derived fluids.

In addition to directly addressing several of the priority science questions outlined in the recent NSF Decadal Survey *Earth in Time*, such as “How are critical elements distributed and cycled through Earth?”, this work serves to contribute to a long-standing discussion among those who study redox processes occurring at convergent margins and beyond.

Chapter 2

1. Introduction

Perhaps one of the most unique aspects of our habitable planet, subduction zones create a large interface between the Earth's crust and mantle and serve to recycle essential materials to the surface. The subduction of hydrated lithosphere contributes to large earthquakes observed at intermediate depths (>50 km) (Hacker et al., 2003; Yamasaki and Seno, 2003), mantle-wedge melting, and arc-magma genesis (Stern, 2002; Rüpke et al., 2004; Codillo et al., 2018) observed at convergent plate margins. As pressure-temperature-depth conditions increase, water-rich minerals in the downgoing plate such as lawsonite undergo dehydration reactions that release fluids and volatiles into the subduction interface. The sulphur, carbon, and iron released during slab devolatilization are also intimately linked to arc-related ore deposits (Sun et al. 2004), and may play a key role in controlling the redox systematics of arc magmas and the deep mantle (Carmichael, 1991; Kelley and Cottrell, 2009; Evans, 2012; Evans and Powell, 2015). One notable geochemical aspect of the mass transfer that occurs at subduction zones is the oxidized nature of arc magmas relative to hot spots and mid-ocean ridges (Kelley and Cottrell, 2009, 2012; Gaborieau et al., 2020). Although some debate exists (Lee et al., 2010; Brounce et al., 2014; Piccoli et al., 2019; Chiaradia, 2021), a leading hypothesis to explain this oxidation is hydrous fluid injection into the mantle wedge of the overriding plate (Kostenko et al., 2002; Konrad-Schmolke et al., 2011; Marschall and Schumacher, 2012).

Hydrated phases within the down going slab mantle and crust, such as serpentine and lawsonite, supply this hydrous fluid to the subduction interface via dehydration reactions that occur with increasing pressure-temperature-depth conditions (Stern, 2002; Fumagalli and Poli,

2005; Hacker, 2008; van Keken et al., 2011; Baxter and Caddick, 2013; Gerrits et al., 2019). The effect these mineral-derived fluids have on the oxidation of both the mafic slab and the overlying mantle wedge, as well as the timescales of their movement, remain a topic of active study. Questions exist largely due to the inaccessibility of these regions and the extremity of conditions under which these geochemical reactions take place.

Recent studies have shown that stable Fe isotopes provide a sensitive record of redox processes occurring within subduction zones (Debret et al., 2016, 2018, 2021; Inglis et al., 2017; Gerrits et al., 2019). Zoned garnets can be receptive passive recorders of fluid release processes that occur during subduction because garnet generally forms in response to progressive dehydration (Baxter and Caddick, 2013). Coupled f_{O_2} and $\delta^{56}\text{Fe}$ measurements across concentrically zoned garnet crystals from subducted high pressure rocks have been shown to display isotopically heavier iron and lower f_{O_2} in garnet rims relative to cores (Gerrits et al., 2019). These results demonstrate that f_{O_2} and Fe fractionation covary within garnet growth conditions and timescales during recrystallization associated with subduction. This phenomenon could be due to the fact that Fe^{2+} is fluid-mobile whereas Fe^{3+} is not. Alternatively, the fractionation could be related to the oxidizing species potentially present in mineral-derived fluids, such as sulfate and chloride. The question of the cause responsible for this observed iron isotope fractionation serves as motivation for this study.

In order to further investigate the question of redox change or fluid mobility, this study will present Fe isotope and Zn isotope data, as Fe isotopes can be fractionated by redox reactions whereas Zn is monovalent and therefore not directly influenced by changing oxidation state. Fe has two oxidation states (Fe^{2+} and Fe^{3+}), with variations between these oxidation states being the primary control on the isotopic fractionation – either through their differences in fluid mobility

or by their reactions to fractionating complexes present in the fluid. By contrast, zinc only has one oxidation state, so isotopic fractionation is entirely controlled by speciation, or the influx or outflux of sulfate- and carbonate-rich fluids capable of mobilizing Zn (Inglis and Moynier, 2021). Thus, the comparison between the two isotope systems should help identify which processes and isotopic signatures are controlled by redox or fluid composition. There are four main co-variations that are likely to occur (Fig. 1), which represent four hypotheses:

1. Only iron isotopes change, signaling that sulfate and carbonate species may not be present in the fluids and that redox is the primary control on fractionation occurring during fluid movement facilitated by subduction (Fig. 1a).
2. Only zinc isotopes vary, showing that sulfate and carbonate species are present in the fluid and maintain primary control on Zn fractionation, yet do not influence Fe fractionation for some reason (Fig. 1b).
3. Iron and zinc fractionation are positively correlated, signaling that sulfate and carbonate species are present in the fluids and influence Zn fractionation, but that another factor must be at play to fractionate Fe in this way (Fig. 1c).
4. Iron and zinc fractionation are negatively correlated, showing that fluids resulting from dehydration reactions fractionate lighter Fe and heavier Zn isotopes than their original source. This demonstrates that the fluids are sulfate- and carbonate-rich and have an effect on the oxidation state of systems they encounter (Fig 1d).

While the co-variation in Fe and Zn isotopes during subduction has been explored between metamorphic facies (Inglis et al., 2017), this study aims to compare Fe and Zn isotopes between four distinct matrix generations. These matrices that crystallized sequentially are related to successive periods of fluid influx that developed in Lago Superiore eclogite breccias within

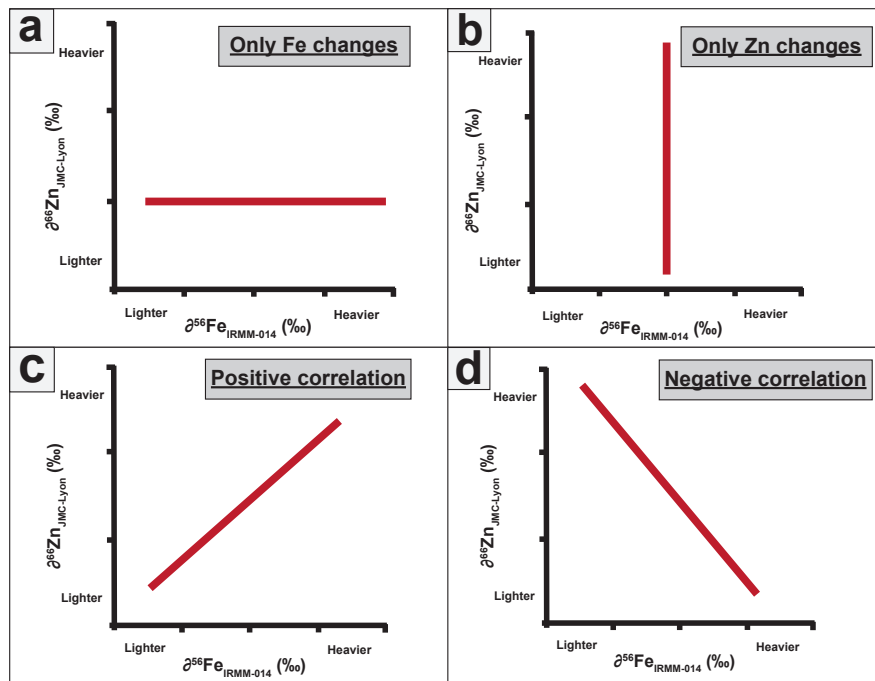


Fig. 1. Iron and zinc isotope analysis hypothesis testing showing hypothetical graphs of data if (a) only iron isotopes change, (b) only zinc isotopes change, (c) iron and zinc have a positive correlation, or (d) iron and zinc have a negative correlation.

the meta-ophiolitic sequence located at Monviso, Italy beginning at peak burial conditions (~80 km) through exhumation to a depth of about 30 km (Angiboust et al., 2012; Locatelli et al., 2018; Agard, 2021). Within these ophiolites are eclogite-facies breccias representing brittle

deformation that occurred at a depth of 80-30 km (Locatelli et al., 2019a). Based on previous geochemical studies, this brittle deformation is thought to have occurred due to high-pressure fluid movement through the mafic, down going slab (Locatelli et al., 2019b). These breccias were then exhumed with delaminated continental crust at the end stages of subduction (Agard, 2021). Although the source of intermediate-depth fluids have been studied extensively (Fumagalli and Poli, 2005; Hacker, 2008; van Keken et al., 2011; Codillo et al., 2018), fluids potentially take different pathways through the mafic slab. Due to the characteristic low permeability of eclogite-facies rocks (Brace, 1984), fluid circulation likely takes place through short-lived, transient conduits (Glodny et al., 2003; Hermann et al., 2006), and probably longer-lived high-strain channels (Konrad-Schmolke et al., 2011; Angiboust et al., 2014; Locatelli et al., 2019b). The exhumation of these rocks likely represents conditions of large-scale fluid

movement and brittle deformation, as suggested by the dissemination of brecciated blocks which are coated in talc, apatite, and garnet-rich metasomatic rinds. Sm-Nd bulk ages of garnets from the metasomatic rind, in conjunction with previously published age data, will provide insights into the rate and duration over which exhumation and related oxidative fluid movement occurred.

2. Background and Geologic Setting

2.1 Redox Conditions at Convergent Boundaries

Arc lavas typically display elevated $\text{Fe}^{3+}/\Sigma\text{Fe}$ relative to ocean island basalts (OIB) and mid-ocean ridge basalts (MORB) (Carmichael, 1991; Behrens and Gaillard, 2006; Kelley and Cottrell, 2009; Brounce et al., 2014). Direct measurement of oxygen fugacity (f_{O_2}) is a difficult parameter to report quantitatively. Kelley and Cottrell (2009) utilized μ -XANES spectroscopy to derive the $\text{Fe}^{3+}/\Sigma\text{Fe}$ and H_2O content of submarine pillow glasses and melt inclusions from a variety of tectonic settings to quantify the degree of oxidation. The combination of these data resulted in a linear correlation between increased ferric iron content and increased water or volatile content in arc magmas as compared to mid-ocean ridge basalts and back-arc basin basalts. This relative oxidation of arc magmas supports the hypothesis that fluids released from hydrous minerals during subduction move through the mafic, down going slab to oxidize the mantle wedge. Despite the link between elevated ferric iron and H_2O content in arc magmas established by Kelley and Cottrell (2009), their interpretation is debated. Lee et al. (2010) argues that since Fe^{3+} is excluded from early mineral crystallization, such as olivine, the upper mantle becomes more oxidized simply due to a progressively increasing $\text{Fe}^{3+}/\Sigma\text{Fe}$ ratio as shallow-level differentiation takes place. MORBs and melt inclusions from the Marianna trough exhibit this ferrous iron partitioning into olivine and clinopyroxene (Brounce et al., 2014), which results in ferric iron enrichment in the melt, with slight changes in f_{O_2} (FMQ +0.1 – FMQ +0.5, where

FMQ is the fayalite-magnetite-quartz buffer; Brounce et al., 2014). Melt inclusions from the Marianna arc, the Sarigan and Alamagan volcanoes, and submarine glasses from Pagan and NW Rota-1 volcanoes, however, all show a significantly more oxidized $\text{Fe}^{3+}/\Sigma\text{Fe}$ than MORB and Marianna trough samples (Brounce et al., 2014). This relationship suggests that the primary mantle-derived source of arc-magmas must be fundamentally different than the primary source of MORB magmas (Brounce et al., 2014). One such difference could be the presence of mafic mineral-derived hydrous fluids that originates from the down going oceanic crust at subduction zones.

One way to investigate the presence and potential nature of fluids within subduction zones involves analyzing the f_{O_2} and iron content of garnet growth zones that formed coeval with the release and movement of these fluids (Gerrits et al., 2019). Thermodynamic modeling with the *Perple_X* (Connolly, 2009) program estimates that the rims of garnets that display lower $\Delta \log \text{FMQ}$ and heavier $\delta^{56}\text{Fe}$ values grew after lawsonite dehydration reactions began (Gerrits et al., 2019). As such, the authors propose lawsonite breakdown as the source of fluids that altered residual mineral assemblages in the mafic slab and consequently altered the iron isotopic composition of garnet growth zones. In this study, we build upon this work by using coupled iron and zinc isotope analysis that aids in the further investigation of the effect hydrous fluids have on isotopic fractionation and system-wide redox state during mineral growth in subduction zones.

Zinc is present in the down-going oceanic crust typically as Zn sulfides or hydrosulfides deposited on the seafloor at mid-ocean ridges, hydrothermal vents, or through biologically facilitated processes (Fujii et al., 2011; Pons et al., 2011). A study of upper-mantle transitional lithologies from the Cerro del Almiraz massif in Spain found an increase of zinc concentrations and heavier $\delta^{66}\text{Zn}$ from Atg-serpentinites to Chl-harzburites (Debret et al., 2021). This variation

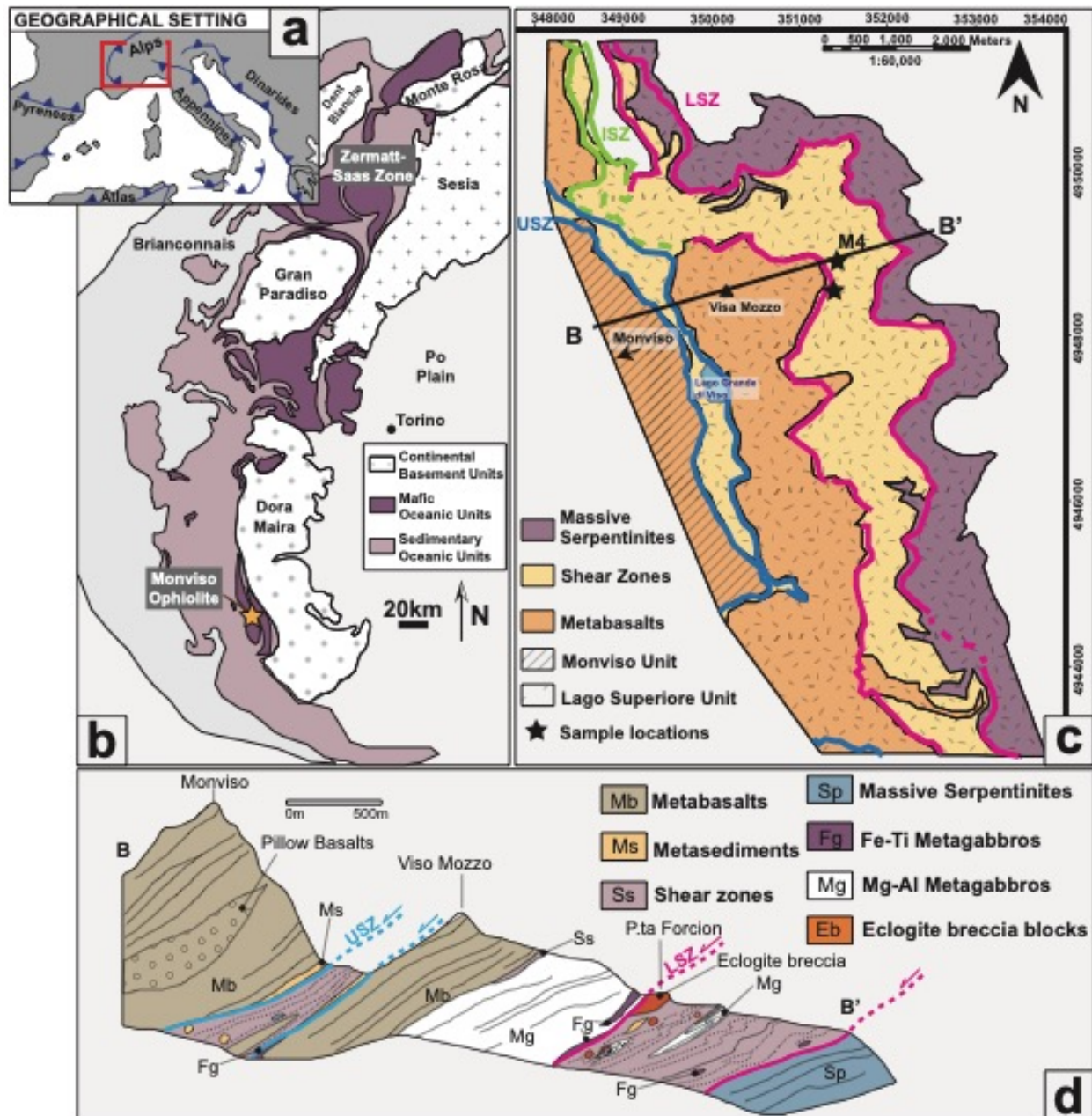


Fig. 2. Geologic maps of the Western Alps and the Monviso Ophiolite. (a) The location of the Alps in Southern Europe. (b) The distribution of continental, mafic, and sedimentary units in the Western Alps, with the orange star showing the specific area of interest; after Starr et al. (2020). (c) A simplified geology sketch of the Lago Superiore and surrounding units, including the location of shear zones; after Locatelli et al. (2019b). (d) Cross-section of the Monviso ophiolite sequence, showing a location of eclogite breccia outcropping and an example of a sampling location; after Locatelli et al. (2019b).

shows that mantle lithologies become enriched in heavy zinc isotopes, with lighter $\delta^{66}\text{Zn}$ values preserved in serpentinites closer to the subduction interface. A decrease in $\delta^{66}\text{Zn}$ values has also

been correlated with a decrease in sulfur content (Pons et al., 2016), suggesting Zn-SO₄²⁻ complexes preferentially incorporate isotopically heavy Zn. As metamorphic grade increases, the release of volatiles contributes to a gradual release of sulfate complexes and isotopically heavy Zn, resulting in a progressive lightening of zinc isotopes in the downgoing serpentinites.

A typical rock experiencing prograde metamorphism during subduction would be expected to undergo a series of dehydration reactions and likely the loss of fluids produced from these reactions. The resulting isotopic signature of the residual rock sample would thus be expected to be influenced by that internal dehydration. By contrast, the Monviso eclogite breccias represent the result of substantial fluid influx. Major and trace element compositions of the different matrix generations suggest that both locally and externally derived fluid sources influenced matrix crystallization (Angiboust et al., 2011; Locatelli et al., 2019b). As a result, we predict that the isotopic signatures are likely controlled by the fluid influx and fluid-rock interactions. By linking Fe and Zn isotopic compositions of each matrix generation with potential fluid sources, we can determine the potential isotopic signature of different fluid types and their redox-influencing capacity.

2.2 The Monviso Ophiolite: A Rock Record of Fluid Movement

Testing the hypothesis that mineral dehydration-derived fluids alter the redox state of mafic material and the overlying mantle wedge is best achieved within oceanic lithosphere that has been subducted and exhumed back to the surface, and shows evidence of fluid infiltration. One locality that preserves large slices of exhumed oceanic lithosphere is the Alpine orogeny, which stretches across the borders of France, Switzerland, and Italy (Fig. 2). The lithosphere of the Tethys, or the Alpine, ocean that subducted during the Alpine orogen – a result of the collision of the Eurasian and Adriatic plates – was a 400-700 km wide, slow spreading, Atlantic-

type seafloor without a magmatic arc (Agard and Handy, 2021). The metamorphic gradient preserved in the Western Alps suggests southeast subduction of the oceanic and European lithosphere underneath the Adriatic plate. Orogenic flysch deposits, or sediment accumulations associated with trench formation, suggest subduction began 100-95 Ma, but no later than 84-86 Ma (Agard and Handy, 2021). Peak burial ages of oceanic fragments occur within 60-40 Ma, and subduction of micro-continents began with the Sesia Zone, continued through the Briançonnais Domain, and ended with the European margin, leading to the collision of Adria and Eurasia. In the Western Alps the sedimentary deposits located to the west display mostly blueschist facies, whereas the mafic and ultramafic units that reached eclogite facies outcrop structurally below and to the east (Agard et al., 2009; Agard, 2021).

The Monviso ophiolite preserves what is widely recognized as one of the world's most intact eclogitized slab fragments. This 15 km long, 2-3 km wide meta-ophiolite, made up of serpentinized ultramafics, Mg-rich metagabbros, and Fe-Ti metagabbros, detached from the downgoing plate at ~80 km depth due to extensive fracturing as evidenced by the eclogite breccias preserved in shear zones (Angiboust et al., 2012; Locatelli et al., 2018). The mafic and ultramafic units in the Western Alps appear to have reached peak burial conditions late in the oceanic subduction history, at most a few million years before continental collision (Agard, 2021). The Monviso peak is divided into two major tectonic units: the blueschist facies Monviso Unit and the eclogite-facies Lago-Superiore unit (Angiboust et al., 2011). The Lago-Superiore unit itself contains two major shear zones: the Intermediate Shear Zone (ISZ), which acts as a boundary between metabasalts and metagabbros, and the Lower Shear Zone (LSZ), which separates metagabbros and the serpentinite sole. Previous geochemical characterization of the serpentinite sole suggests the majority of the hydrothermal alteration of the mantle occurred on

the seafloor (Angiboust et al., 2014; Gilio et al., 2020). Fe-Ti metagabbro outcroppings in the ISZ display mylonitization with the planar fabric dominated by an omphacitic clinopyroxene, garnet, and rutile assemblage (Angiboust et al., 2014). Fe-Ti metagabbro mylonites found along ISZ can also be observed embedded within the serpentinite sole below the LSZ. These metagabbros, which have extremely similar P-T paths to one another (Angiboust et al., 2014), have experienced a subduction-parallel shearing history of coupled ductile and brittle deformation (Locatelli et al., 2019b).

The Lower Shear Zone marks the interface between rheologically strong gabbros and weak serpentinitized oceanic mantle and can be continuously traced from N-S for about 15 km. The eclogite breccias and eclogite-facies metasomatic rinds that rim brecciated blocks present within the LSZ signify that this shear zone was active during eclogite-facies metamorphism at a depth of about 75-85 km (Angiboust et al., 2014). This deformation was accompanied by block disaggregation and rotation, which resulted in the block-in-matrix structure observable in the LSZ today (Locatelli et al., 2018). West-dipping mylonitic foliation is visible in the hanging wall and is the product of ductile deformation along the LSZ. Fe-Ti metagabbros within the LSZ are considered ideal material to study fluid movement because they display very little evidence of seafloor hydration – such as carbonate enrichments – which makes them more likely to record hydration during fluid-assisted recrystallization (Angiboust et al., 2014). The eclogitic metagabbro blocks in the LSZ, encompassing both Mg-Al and Fe-Ti metagabbros, can be classified as one of three block types based on their structural and mineralogical properties (Locatelli et al., 2019a).

The progressive development of the eclogitic breccia block types is discernable by three distinct matrix generations that entrain the mylonitic metagabbro clasts and are relatively

undeformed (Fig. 3; Locatelli et al., 2018). M1 is omphacite-rich and signals the onset of brecciation. The second generation, M2, contains garnet as well as omphacite. M3 sees the addition of lawsonite to the omphacite and garnet assemblage, which is then altered locally by metasomatism to crystallize newly-formed garnet, talc, chlorite, amphibole, and Ca-rich diopside. M3 is the volumetrically dominant matrix type and contains up to ~40 vol% of lawsonite in places. In comparison to the relatively anhydrous matrices M1 and M2, the presence of a hydrous mineral phase in M3 suggests that external fluid began to infiltrate the area in the late stages of brecciation. The fourth matrix type (M4) exists as a garnet-rich talc and apatite mesh (Fig. 3) that rims large brecciated blocks that are disseminated within the antigorite schists of the LSZ.

Garnets within the mylonitized clasts present in the Monviso eclogite breccias display a series of cross-cutting fracture populations (Broadwell et al., 2019), which is another indication that fluid infiltrated through the LSZ. The two fracture populations are distinguishable mainly by their Mn and Fe contents. The low-Mn and high-Fe fractures often truncate within the garnet crystal against high-Mn rims, signaling that perhaps these fractures formed before the end of garnet growth. The high-Mn fractures often bifurcate the entire crystal and cross over the low-Mn fractures (Broadwell et al., 2019). The mylonitic fabric suggests that deformation began ductilely, but fractures within Fe-Ti metagabbro-derived garnet crystals show that brittle deformation occurred subsequent to ductile behavior but prior to peak metamorphism. The occurrence of these fractures exclusively within brecciated clasts tells us that a brittle deformation event occurred during prograde subduction and prior to detachment of the slab. The fact that these healed garnet fractures have a different composition than the host garnet implies a free fluid phase at least transiently present during brittle deformation events (Broadwell et al.,

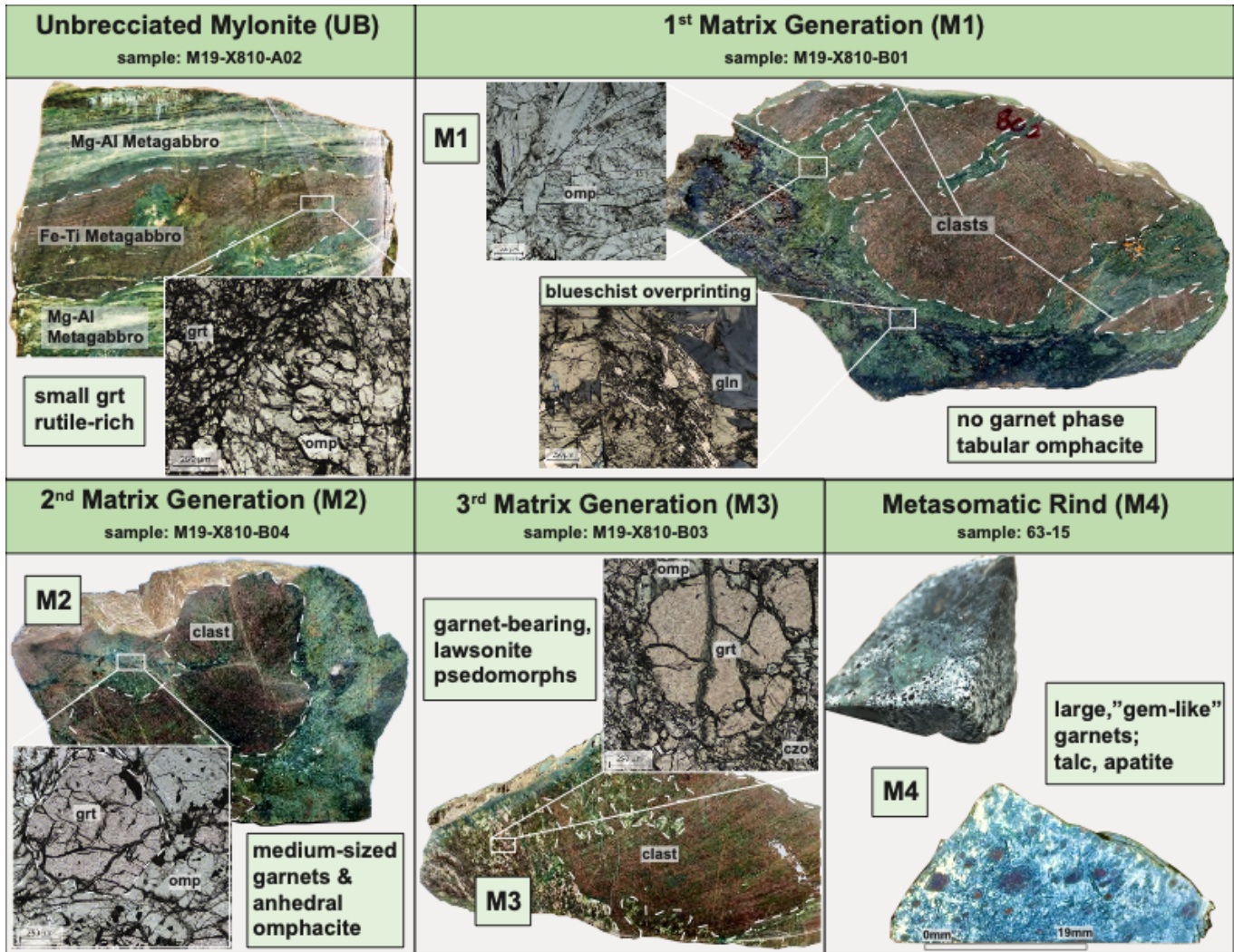


Fig. 3. Hand sample and thin section photos of the samples used in this study. All samples were collected below the upper limit of the Lower Shear Zone (LSZ). The unbrecciated mylonite likely represents prograde ductile deformation, while the M1 through M4 samples represent successive periods of brittle deformation, fluid flux, and exhumation. All samples shown here were used for iron and zinc analysis, and M4 was used for Sm-Nd garnet geochronology.

2019). *In-situ* stable oxygen isotope analysis suggests the fluid responsible for these garnet fractures was locally derived, although later matrix generations and metasomatic rinds also imply the presence of a fluid derived from the serpentinite sole below (Rubatto and Angiboust, 2015). Concordant with the observation from Locatelli et al. (2018), these data show that most of the eclogite breccias are located near a major lithological contact that acted as a fluid-focusing structure. The LSZ channeled the fluid produced from dehydration reactions in neighboring

lithologies and rapidly increased the fluid pore pressure – either facilitating fracture or focused in the LSZ due to fracturing (Locatelli et al., 2019b).

3. Sample Descriptions

All samples presented in this study were collected below the upper limit of the LSZ (Fig. 2), among a concentration of brecciated blocks within mylonitic serpentinite schists. The first sample (Fig. 3), hereby known as the unbrecciated mylonite, is a mylonitized Mg-Al, Fe-Ti metagabbro. The Fe-Ti metagabbro component is visually discernable at hand sample scale by the red-brown color, and was separated using the rock saw. The M1 sample comes from a large, Fe-Ti-metagabbro-clast rich block with M1 being the dominant matrix. This block also displays edges rich in glaucophane, representing a period of blueschist overprinting during exhumation. The M2 matrix sample (Fig. 3), the first matrix generation to present a significant proportion of garnet, comes from a smaller block with the clast material concentrated in the center. The M3 sample comes from a block with slightly more disaggregated clast material (Fig. 3) and white-colored lawsonite pseudomorphs, determined to be clinozoisite, that are visible in hand sample, along with garnet and omphacite phases. This M3 sample is uncharacteristically enriched in garnets as compared to previous studies (Locatelli et al., 2018). The final matrix generation M4 (Fig. 3), also referred to as the metasomatic rind, was previously sampled and geochemically investigated as sample 63-15 (Locatelli et al., 2018). M4 replaces the eclogite-facies assemblage with a mesh of talc, chlorite, distinct brown metasomatic garnet, and acicular amphibole and diopside (Locatelli et al., 2018). The garnets analyzed in this study originate from matrix generations, and are distinct from garnets within the unbrecciated mylonite and the mylonitized clasts that the matrix generations entrain.

4. Methods

Pyroxene Group																			
Clast																			
Mineral	SiO ₂	TiO ₂	Al ₂ O ₃	Cr ₂ O ₃	FeO _T	MnO	MgO	CaO	Na ₂ O	K ₂ O	Total	Mg #	XW _o	XEn	XF _s	XQuad	XJd	XAe	Total
Omphacite	56.11	0.1374	6.223	0.0600	7.680	0.0483	10.26	16.05	5.951	0.000	102.5	0.70	0.29	0.26	0.01	0.56	0.25	0.19	99.93
Omphacite	56.64	0.0489	6.788	0.0089	7.691	0.0785	9.819	15.06	6.256	0.000	102.4	0.69	0.28	0.25	0.03	0.56	0.28	0.16	99.99
Omphacite	55.46	0.0676	5.497	0.0405	8.148	0.0090	10.13	15.83	5.919	0.000	101.1	0.69	0.29	0.26	0.01	0.56	0.22	0.21	99.95
Aegyrine-augite	55.40	0.0813	4.242	0.0049	7.740	0.0000	11.80	17.65	4.814	0.006	101.7	0.73	0.32	0.30	0.01	0.62	0.17	0.21	100.0
Aegyrine-augite	54.93	0.0062	3.020	0.0121	10.636	0.1263	10.32	18.48	4.148	0.000	101.7	0.63	0.35	0.27	0.06	0.69	0.13	0.19	99.99
Diopside	55.30	0.0178	2.066	0.0245	6.200	0.0606	14.12	21.43	2.627	0.004	101.9	0.80	0.39	0.36	0.02	0.78	0.08	0.14	99.99
Diopside	55.81	0.0000	3.062	0.0692	4.173	0.0183	14.85	20.99	2.780	0.000	101.8	0.86	0.38	0.38	0.01	0.77	0.12	0.11	99.96
Omphacite	56.04	0.0000	3.290	0.0337	4.814	0.0000	13.96	21.13	3.179	0.000	102.4	0.84	0.38	0.35	0.01	0.74	0.13	0.13	99.98
M1																			
Mineral	SiO ₂	TiO ₂	Al ₂ O ₃	Cr ₂ O ₃	FeO _T	MnO	MgO	CaO	Na ₂ O	K ₂ O	Total	Mg #	XW _o	XEn	XF _s	XQuad	XJd	XAe	Total
Omphacite	54.73	0.049	6.979	0.894	6.249	0.000	9.010	13.79	6.521	0.000	98.22	0.72	0.27	0.24	0.02	0.55	0.30	0.14	98.85
Omphacite	54.56	0.047	7.462	0.855	5.920	0.000	8.900	13.74	6.818	0.002	98.31	0.73	0.26	0.23	0.00	0.51	0.31	0.17	98.83
Omphacite	55.17	0.034	7.321	0.964	6.119	0.000	8.883	13.73	6.687	0.020	98.93	0.72	0.26	0.24	0.02	0.54	0.31	0.14	98.74
M2																			
Mineral	SiO ₂	TiO ₂	Al ₂ O ₃	Cr ₂ O ₃	FeO _T	MnO	MgO	CaO	Na ₂ O	K ₂ O	Total	Mg #	XW _o	XEn	XF _s	XQuad	XJd	XAe	Total
Omphacite	55.95	0.0147	6.411	0.0053	7.646	0.016	9.985	15.15	6.182	0.006	101.4	0.70	0.28	0.26	0.02	0.55	0.26	0.19	99.99
Omphacite	55.27	0.0574	5.547	0.0465	8.115	0.013	10.40	16.19	5.551	0.000	101.2	0.70	0.30	0.26	0.02	0.58	0.22	0.20	99.95
Omphacite	55.28	0.0260	5.840	0.0564	8.286	0.000	10.27	15.95	5.880	0.000	101.6	0.69	0.29	0.26	0.00	0.55	0.23	0.22	99.93
Omphacite	55.82	0.0611	6.607	0.0662	7.629	0.020	9.889	15.48	6.258	0.000	101.8	0.70	0.28	0.25	0.01	0.53	0.26	0.20	99.92
Omphacite	55.94	0.0372	6.696	0.0273	7.696	0.000	9.959	14.96	6.023	0.000	101.3	0.70	0.28	0.26	0.03	0.57	0.27	0.16	99.97
Omphacite	55.90	0.0270	7.405	0.0035	6.868	0.052	9.514	14.63	6.573	0.000	101.0	0.71	0.27	0.24	0.01	0.52	0.30	0.18	100.0
Omphacite	55.79	0.0243	5.240	0.0226	6.932	0.030	11.29	16.80	5.286	0.000	101.4	0.74	0.31	0.29	0.01	0.61	0.21	0.18	99.98
M3																			
Mineral	SiO ₂	TiO ₂	Al ₂ O ₃	Cr ₂ O ₃	FeO _T	MnO	MgO	CaO	Na ₂ O	K ₂ O	Total	Mg #	XW _o	XEn	XF _s	XQuad	XJd	XAe	Total
Aegyrine-augite	53.01	0.030	2.609	0.001	8.182	0.089	11.51	19.40	3.245	0.000	98.08	0.71	0.38	0.31	0.04	0.73	0.11	0.16	100.0
Aegyrine-augite	53.48	0.035	3.724	0.024	7.953	0.058	10.96	17.80	4.095	0.030	98.16	0.71	0.34	0.30	0.04	0.68	0.16	0.16	99.98
Aegyrine-augite	53.03	0.043	2.724	0.010	6.927	0.000	12.32	19.29	3.112	0.006	97.46	0.76	0.38	0.33	0.04	0.75	0.12	0.14	99.99
Aegyrine-augite	53.03	0.008	2.309	0.001	6.562	0.004	12.57	19.94	2.930	0.006	97.36	0.77	0.39	0.34	0.03	0.76	0.10	0.14	100.0
Aegyrine-augite	53.38	0.030	3.908	0.006	7.185	0.017	11.25	17.83	4.210	0.015	97.83	0.74	0.34	0.30	0.02	0.66	0.16	0.17	99.99
Garnet Group																			
Clast																			
Mineral	SiO ₂	TiO ₂	Al ₂ O ₃	Cr ₂ O ₃	FeO _T	MnO	MgO	CaO	Na ₂ O	K ₂ O	Total	Mg #	XAlm	XPrp	XGr _s	Total			
Almandine	38.69	0.059	21.97	0.000	28.14	0.935	3.811	9.232	0.000	0.002	102.8	0.19	0.59	0.15	0.23	96.0			
Almandine	38.06	0.006	21.46	0.000	28.31	0.659	3.068	10.33	0.027	0.000	101.9	0.16	0.59	0.12	0.25	95.4			
Almandine	38.31	0.062	21.24	0.011	28.80	0.720	2.303	10.15	0.026	0.034	101.7	0.12	0.61	0.09	0.26	96.3			
Almandine	38.48	0.095	21.49	0.000	27.22	0.484	4.202	9.780	0.034	0.000	101.8	0.22	0.56	0.16	0.23	95.9			
Almandine	38.43	0.094	21.61	0.030	27.95	1.039	2.693	10.50	0.030	0.000	102.4	0.15	0.59	0.10	0.26	95.4			
M1																			
Mineral	SiO ₂	TiO ₂	Al ₂ O ₃	Cr ₂ O ₃	FeO _T	MnO	MgO	CaO	Na ₂ O	K ₂ O	Total	Mg #	XAlm	XPrp	XGr _s	Total			
Almandine	37.31	0.028	20.68	0.170	27.04	0.264	6.430	6.087	0.000	0.024	98.03	0.30	0.57	0.25	0.13	95.5			
Almandine	37.67	0.061	20.70	0.714	25.90	0.079	6.767	6.803	0.000	0.000	98.70	0.32	0.55	0.27	0.14	94.9			
Almandine	37.21	0.023	20.95	0.230	27.04	0.058	6.779	5.795	0.015	0.031	98.13	0.31	0.57	0.27	0.12	96.2			
Almandine	38.06	0.074	20.29	0.647	26.22	0.058	6.416	6.804	0.000	0.000	98.57	0.30	0.56	0.25	0.14	94.4			
Almandine	37.63	0.027	20.65	0.560	26.84	0.082	6.593	5.866	0.012	0.000	98.26	0.30	0.58	0.26	0.12	95.9			
Almandine	37.61	0.070	20.90	0.475	26.19	0.089	6.444	6.738	0.000	0.000	98.52	0.30	0.56	0.25	0.15	96.1			
Almandine	37.56	0.039	20.33	0.507	26.06	0.114	6.741	6.381	0.016	0.000	97.75	0.32	0.55	0.27	0.13	95.0			
M2																			
Mineral	SiO ₂	TiO ₂	Al ₂ O ₃	Cr ₂ O ₃	FeO _T	MnO	MgO	CaO	Na ₂ O	K ₂ O	Total	Mg #	XAlm	XPrp	XGr _s	Total			
Almandine	38.58	0.055	21.87	0.057	28.06	0.268	5.755	6.827	0.004	0.024	101.5	0.27	0.59	0.22	0.17	97.6			
Almandine	38.15	0.048	21.48	0.004	28.27	0.393	5.923	7.105	0.024	0.000	101.4	0.27	0.58	0.23	0.15	95.1			
Almandine	38.69	0.092	21.68	0.058	28.12	0.392	5.961	6.842	0.041	0.000	101.9	0.27	0.58	0.23	0.15	96.2			
Almandine	38.94	0.049	21.84	0.040	28.04	0.431	6.016	6.318	0.003	0.000	101.7	0.28	0.59	0.23	0.16	97.6			
Almandine	38.53	0.007	21.72	0.033	28.86	0.589	5.866	6.172	0.032	0.000	101.8	0.27	0.60	0.22	0.14	96.1			
Almandine	38.72	0.043	21.49	0.019	28.98	0.423	5.716	6.162	0.012	0.000	101.6	0.26	0.61	0.22	0.14	96.6			
Almandine	38.39	0.000	21.98	0.037	28.93	0.663	6.030	5.658	0.018	0.024	101.7	0.27	0.61	0.23	0.13	96.6			
M3																			
Mineral	SiO ₂	TiO ₂	Al ₂ O ₃	Cr ₂ O ₃	FeO _T	MnO	MgO	CaO	Na ₂ O	K ₂ O	Total	Mg #	XAlm	XPrp	XGr _s	Total			
Almandine	37.49	0.047	20.59	0.028	24.83	0.557	2.553	12.89	0.017	0.000	99.00	0.15	0.53	0.10	0.33	95.2			
Almandine	37.39	0.092	20.35	0.032	25.08	0.589	2.674	12.45	0.039	0.000	98.70	0.16	0.53	0.11	0.31	94.5			
Almandine	37.89	0.095	20.16	0.049	25.23	0.701	2.511	12.81	0.000	0.002	99.45	0.15	0.52	0.10	0.31	93.0			
Almandine	37.05	0.152	19.71	0.019	24.99	0.751	2.388	13.70	0.014	0.004	98.78	0.15	0.51	0.10	0.31	91.1			
Almandine	37.00	0.052	20.32	0.000	25.84	0.713	2.852	12.10	0.018	0.010	98.90	0.16	0.54	0.11	0.28	93.1			
Almandine	37.64	0.065	19.85	0.000	26.51	0.503	2.844	11.82	0.013	0.029	99.28	0.16	0.54	0.11	0.27	92.4			
Almandine	37.80	0.183	19.93	0.007	22.49	0.328	2.219	15.65	0.000	0.002	98.61	0.15	0.46	0.09	0.38	93.1			

Table 1. A representative sample of oxide data generated from CAMECA SX-Five microprobe at ISTeP, UMPC in Paris, France used to generate the ternary diagrams in Fig. 4.

4.1 Microprobe Analysis

The four samples of brecciated blocks described above were cut and drilled to separate the target lithologies from one another and from the clasts. Thin section scale characterization of each matrix generation was performed using both optical microscope and scanning electron microscope (SEM) analysis (Boston College Center for Isotope Geochemistry). Mineral chemical compositions were then analyzed by electron probe microanalyzer (EPMA) (CAMECA SX-Five; ITeP, UMPC, Paris) with analytical conditions for spot analysis of 15 kV, 40 nA, wavelength-dispersive spectroscopy (WDS) mode. Standards used were Fe₂O₃ (Fe), MnTiO₃ (Mn, Ti), diopside (Mg, Si), CaF₂ (F), orthoclase (Al, K), anorthite (Ca) and albite (Na). FeO was assumed to represent the FeO-total, with Fe³⁺ recalculated based on stoichiometry and charge balance for ferric-iron bearing minerals. The collected oxide data was used to calculate the structural formulas of garnet and omphacite (Table 1), which were then compared to previous analysis (Locatelli et al., 2019b).

4.2 Iron and Zinc Isotopes

Stable iron and zinc isotope measurements were made on the following: (1) ‘bulk’ separates of the different of matrix types consisting of all of the minerals in the matrix; and (2) separated garnets fractions for matrix types containing garnet (unbrecciated mylonite, M2, M3, and M4). The different matrix generations were drilled out and separated utilizing a New Wave MicroMill (Pollington and Baxter, 2011). After extensive petrographic investigation, later confirmed with microprobe analysis, billets corresponding to the M1, M2, and M3 matrix types were cut into 2 mm thick slices using a microsaw, mounted on a graphite block with crystal bond, secured within a Teflon ring, and attached to a sample stage. The different matrix generations were then drilled out as solid separated pieces utilizing a New Wave MicroMill

(Pollington and Baxter, 2011). This study utilizes ~800 μm thick diamond particle drill bits due to the hardness of garnet and eclogite-facies rocks.

The separated bulk matrix and garnet separated were then fully dissolved in concentrated HF (< 200 μl), concentrated HNO_3 , aqua regia, and finally 1.5M HBr. The aqua regia stage of dissolution is especially important, since Zn is likely to partition into the fluoride phase as ZnF_2 (Inglis et al., 2017) and aqua regia is especially effective at dissolving fluorides. Hydrochloric acid has also been found to fractionate zinc isotopes (Fujii et al., 2010), so Zn chemical separation procedures were performed using hydrobromic acid. The Zn purification protocol, which takes place first, employs an anion AG-1 X8 (200-400 mesh) exchange resin in Teflon 1:4 shrinkage tubes, with a resin volume of 500 μl . The small column size serves to reduce the amount of resin and acid the sample comes into contact with, therefore reducing the blank (van Kooten and Moynier, 2019). These chemical separation methods have been estimated to produce a blank of < 7% of a 5 ng Zn sample (van Kooten and Moynier, 2019). The matrix elution from the Zn separation is collected and then subjected to Fe purification processes. Cleaned AG-1 X8 (200-400 mesh) resin is used to separate Fe from the Zn matrix fraction. For Fe purification we used a larger column with a resin volume of ~1.2 mL, a reservoir basin of ~10 mL, and utilizing an HCl medium (Williams et al., 2009; Inglis et al., 2017). Samples are loaded in 6M HCl, the matrix washed in 6M HCl and then Fe quantitatively eluted in 0.4N HCl. Because Fe is a major element in all of the samples measured here, the blank contribution is highly unlikely to be problematic.

Measurements of the purified Fe and Zn fractions were then performed with a multiple-collector (MC) ICP-MS (Thermo Scientific Neptune Plus) at the Institut de Physique du Globe de Paris (IPGP). Variations of stable isotopes within an earth material are typically reported

using delta notation, which compares a measured isotopic ratio with a well-known standard – in

this case IRMM-014 for Fe – $\left(\frac{\frac{56Fe}{54Fe}_{sample}}{\left(\frac{56Fe}{54Fe}_{IRMM-014} - 1 \right)} \right) \times 10^3$ – and JMC-Lyon for Zn –

$\left(\frac{\frac{66Zn}{64Zn}_{sample}}{\left(\frac{66Zn}{64Zn}_{JMC-Lyon} - 1 \right)} \right) \times 10^3$. There are four naturally occurring Fe isotopes and five naturally

occurring Zn isotopes. For both Fe and Zn the instrumental mass bias is corrected using the standard sample bracketing technique (Inglis et al., 2017; Mason et al., 2004).

4.3 Sm-Nd Garnet Geochronology

The garnet-bearing metasomatic rind (M4) was also used to conduct Sm-Nd garnet geochronology to constrain this latest stage fluid passage and the duration of brecciation and fluid flow. In preparation, the rind was separated from the block using a rock saw, crushed with an agate mortar and pestle, and magnetically separated with a Frantz Isodynamic Separator. Garnets were then carefully hand-picked from the magnetic fraction and crushed to 75-150 μm , hereby referred to the Gt D fraction. Anything crushed to a grain size of $< 75 \mu\text{m}$ was separated and described as the powdered fraction (labelled Gt D Pwd), and were subsequently dissolved and analyzed separately. Garnets are dated utilizing the isochron method (Baxter and Scherer, 2013). Since micro-inclusions within garnet crystals typically contain Sm and Nd in concentrations that are orders of magnitude greater than their host mineral, their removal is essential to a precise and accurate representation of the garnet age. This removal is achieved through a process known as “partial dissolution,” described in detail by Starr et al. (2020). This process involved adding low concentration HF to the garnet separates for two hours at 120°C in order to dissolve silicate inclusion phases (as well as part of the garnet separate). This was followed by two hours in HNO₃ at 120°C to dissolve fluorides produced in the preceding HF

step. This two stage HF + HNO₃ process was repeated 2-3 times until the majority of the residue had been dissolved (70-90% total weight loss). The HF + HNO₃ leachates produced during each 2 stage partial dissolution stage were then retained and labelled according to the number of HF + HNO₃ dissolution stages (Lch 1, Lch2, etc). The Gt D fractions yielded three leachates and the Gt D Pwd fractions yielded two leachates. These leachates contain a mixture of dissolved garnet and inclusions and are expected to get progressively cleaner (i.e. with less inclusions) with each HF + HNO₃ dissolution stage as more inclusions are removed (Starr et al., 2020) The material left after all leaches is referred to as the residues, and theoretically should be the cleanest, or most inclusion-free, fractions analyzed. Following the dissolution of micro-inclusions, all samples are fully dissolved using HF + HNO₃ + HCl, spiked with a well calibrated and mixed ¹⁴⁷Sm-¹⁵⁰Nd tracer, and run through 3-step column chemistry to isolate Sm and Nd (Harvey and Baxter, 2009; Starr et al., 2020). The Sm and Nd fractions were then measured using an IsotopX Phoenix Thermal Ionization (TI) MS at the Boston College Center for Isotope Geochemistry. An in-house 4 ng Nd standard (Ames metal) was routinely measured over the course of the study and yielded a mean ¹⁴³Nd/¹⁴⁴Nd value of 0.512156 ± 0.0000090 (2SD; n = 17). This external reproducibility of the standard was used in age calculations for analyses in which the internal run precision was greater than the external value. Nd column blanks measured over the course of this study did not exceed 2.8 pg of Nd, and were thus deemed not significant for age calculations. The garnets were then dated using isochrons constructed from a combination of garnet residues, leachates, and whole rock points.

5. Results

5.1 Microprobe Results

Garnet and clinopyroxene EPMA analyses for the unbrecciated mylonite (UB), clasts, and the M1, M2, and M3 matrix generations are shown in Table 1 and Figure 4, with a comparison to the compositional ranges measured in Locatelli et al. (2018). Both garnet and clinopyroxene analyses shows considerable variation in compositions, with different lithologies (UB, clasts, M1, M2, and M3) generally falling within distinctly different compositional ranges. All five lithologies that were analyzed correspond well to the previously established compositional ranges described in Locatelli et al. (2018) (Fig. 4). A notable exception is the composition of the M3 garnets which are more grossular rich than the previously measured ones (Fig. 4). However, the analyzed M3 omphacites fit within the expected range, and this matrix

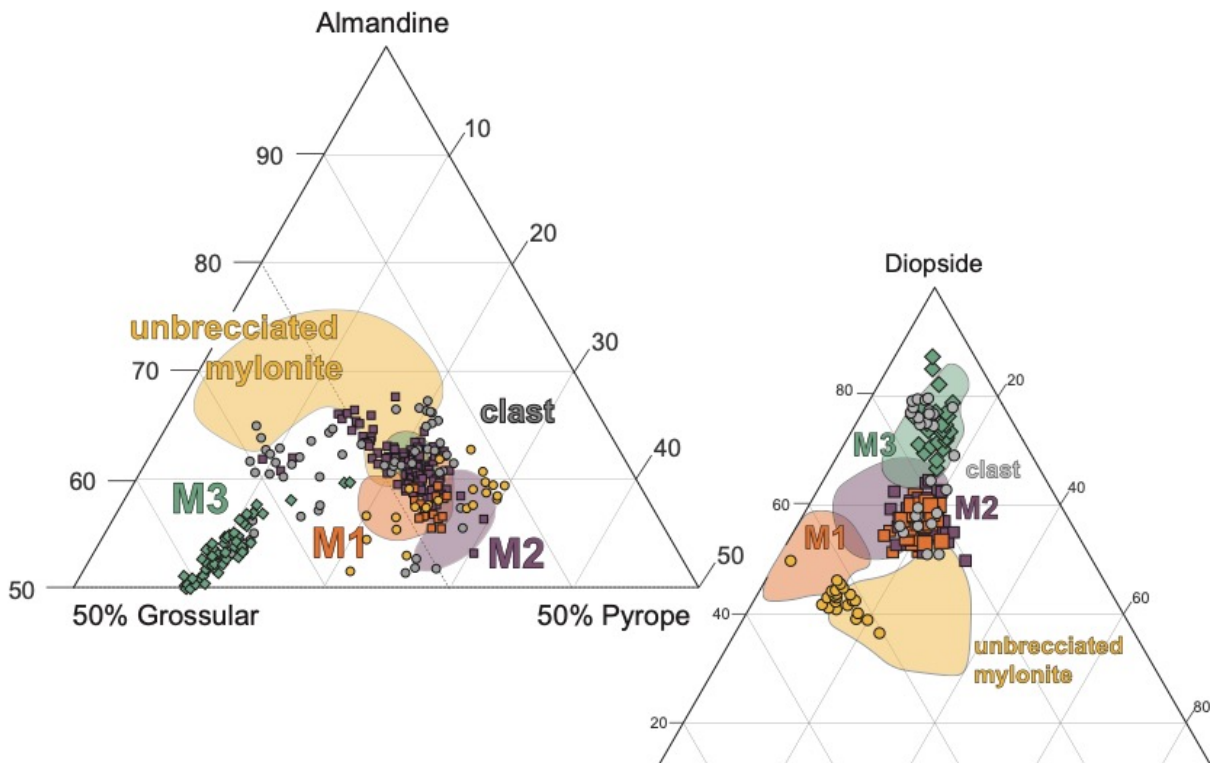


Fig. 4. Ternary diagrams showing the results of microprobe spot analysis of garnet (left) and omphacite (right), as compared to previously published ranges, shown by the shaded regions (Locatelli et al., 2018). The ratios of almandine-grossular-pyrope and diopside-jadeite-aegirine were calculated using oxide data collected with the SXFive microprobe at IStEP, UMPC, Paris.

type is very mineralogically distinctive, containing high modal abundances of coarse grained lawsonite, suggesting that the M3 classification for M19-X810-B03 was correct. The variation in garnet compositions may indicate some variation in the original protolith prior to M3 matrix formation and metasomatism.

5.2 Iron and Zinc Isotope Results

The whole-rock and garnet Fe isotope compositions are reported as $\delta^{56}\text{Fe}$ and all errors as two standard deviations (2σ) of repeat analyses of the same sample aliquot. The $\delta^{56}\text{Fe}$ values are presented in Table 2a. The range of $\delta^{56}\text{Fe}$ values for all samples analyzed here is between $0.43 \pm 0.06\text{‰}$ and $-0.25 \pm 0.07\text{‰}$ reflecting significant variation, particularly compared to previous variation in high-pressure metamorphic rocks (Debret et al., 2016, 2021; Inglis et al., 2017; Gerrits et al., 2019). The whole-rock fractions range from $0.43 \pm 0.06\text{‰}$ to $-0.13 \pm 0.05\text{‰}$; the

a) Fe and Zn Isotopes

Matrix Generation	$\delta^{56}\text{Fe}$	2sd	$\delta^{66}\text{Zn}$	2sd
UB WR	0.19	0.01	-0.27	0.06
UB GRT	-0.1	0.03		
M1 WR	0.43	0.06	-0.60	0.03
M1 BS	0.31	0.04	-0.48	0.04
M2 WR	0.23	0.05	-0.45	0.06
M2 GRT	-0.25	0.07		
M3 WR	0.23	0.04	-0.67	0.07
M3 GRT	0.16	0.04		
M4 WR	-0.13	0.05	-0.82	0.07
M4 GRT	-0.21	0.04		

b) Sm-Nd Garnet Geochronology

Sample Name	$^{147}\text{Sm}/^{144}\text{Nd}$	2 S.E.	$^{143}\text{Nd}/^{144}\text{Nd}$	2 S.E.	Nd error ppm	Nd (ppm)	Sm (ppm)
M4 WR	0.262833	0.000062	0.513124	0.000004	8.2	5.68	2.47
Gt D lch 1	0.772630	0.000100	0.513272	0.000007	12.8	2.04	2.61
Gt D lch 2	1.812471	0.000505	0.513564	0.000025	48.5	0.755	2.26
Gt D lch 3	4.487299	0.001075	0.514278	0.000013	24.3	0.277	2.05
Gt D ALQ 1	3.513827	0.000761	0.513703	0.000016	32.0	0.377	2.19
Gt Pwd 3 lch 1	0.757315	0.000137	0.513276	0.000011	22.3	1.93	2.41
Gt Pwd 3 lch 2	1.076203	0.000157	0.513365	0.000010	19.7	1.19	2.11
Gt Pwd 3 residue	3.245703	0.000757	0.514047	0.000023	44.2	0.401	2.15

Table 2. Isotope data: (a) Iron and zinc isotopes generated with the MC-ICP-MS at the Institut de Physique du Globe de Paris (IPGP). (b) Measured Sm-Nd ratios and errors generated with the TIMS at the Boston College Center for Isotope Geochemistry.

garnet fractions, from $0.16 \pm 0.04\text{‰}$ to $-0.25 \pm 0.07\text{‰}$. The glaucophane-rich, blueschistoverprint fraction displays the highest $\delta^{56}\text{Fe}$ value at $0.43 \pm 0.06\text{‰}$, while the UB through M3 whole rock fractions are fairly well clustered around $0.43\text{-}0.23$ and mostly fall within error of each other (Fig. 5a). Of the whole-

rock fractions analyzed, M4 is considerably different from all other values with a much lighter iron isotopic signature ($-0.13 \pm 0.05\%$). The garnet fractions (Fig. 5b) indicate a less-clear trend, with M3 being the most distinct, heaviest $\delta^{56}\text{Fe}$ value of $0.16 \pm 0.04\%$.

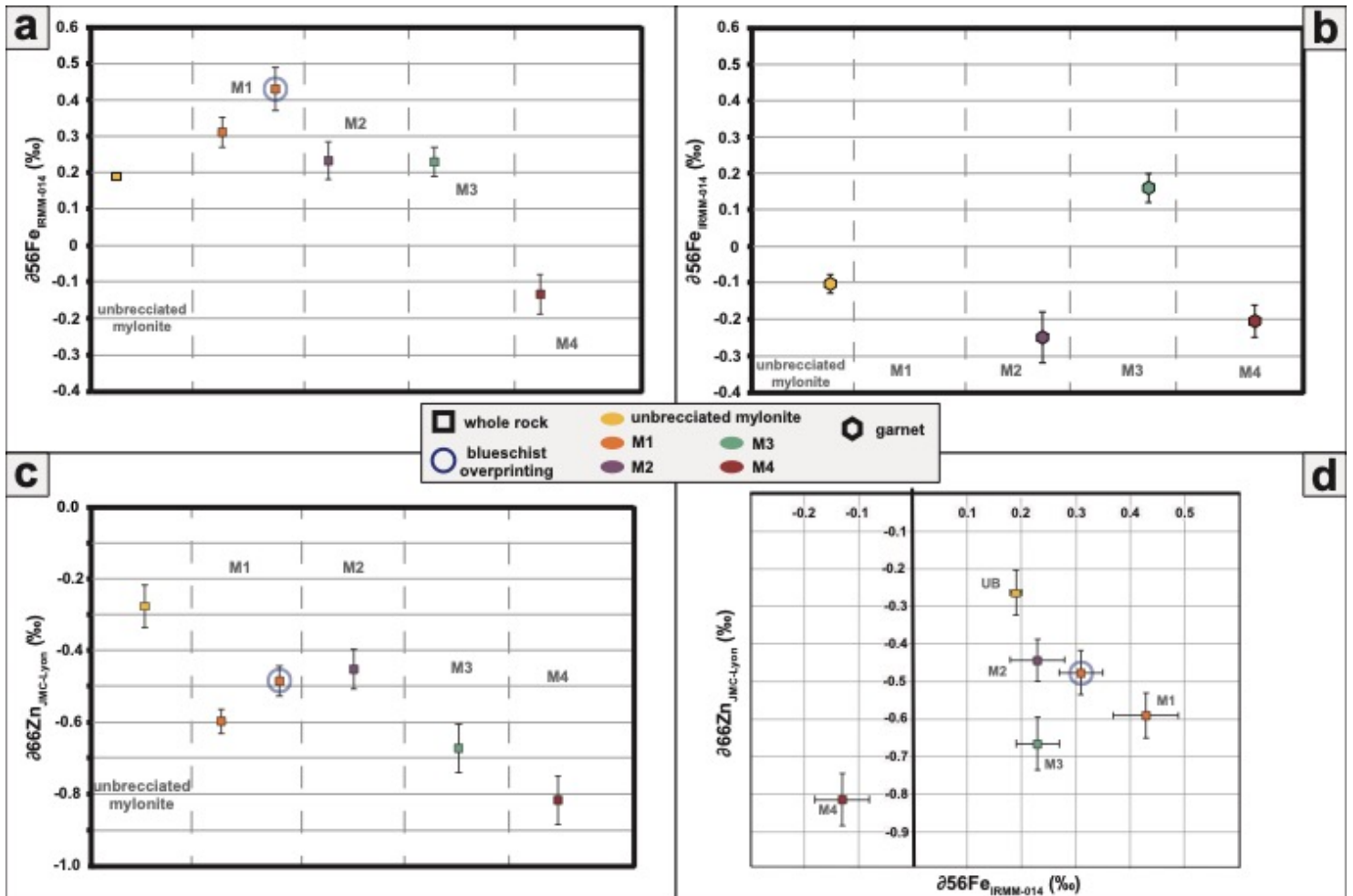


Fig. 5. Iron and zinc isotopic compositions as they vary between matrix generations that represent successive periods of fluid flux, brittle then ductile deformation, and exhumation (Fig. 4a-c). (a) Whole-rock $\delta^{56}\text{Fe}$ variation through time, as interpreted through structural relationships between matrix generations, with the exception of the point representing blueschist overprinting. Iron isotopic variation shows a pattern of progressive lightening as retrograde metamorphism, fluid flux, and exhumation occurs. (b) Garnet $\delta^{56}\text{Fe}$ variation through time. Iron isotopic variation within the garnets is not as clear, with M3 garnets displaying the most unique isotopic signature of the four garnet-bearing matrices. (c) Whole-rock $\delta^{66}\text{Zn}$ isotopic variation through time. Zinc isotopic variation also shows a general isotopic lightening, with M4 once again resulting in the lightest isotopic signature. (d) Graph showing $\delta^{56}\text{Fe}$ vs. $\delta^{66}\text{Zn}$ for each matrix generation. This graph could be interpreted as a bimodal distribution with M4 being the only clearly distinct event, or as two separate trends, one with a negative correlation (UB to M2) between the isotopic systems and one with a positive correlation (M2 to M4).

The whole-rock Zn isotope compositions are reported as $\delta^{66}\text{Zn}$, with all errors again being given as 2σ of n . The $\delta^{66}\text{Zn}$ values of all samples analyzed are reported alongside Fe isotope compositions in Table 2a. The range of $\delta^{66}\text{Zn}$ values for all samples analyzed here is between $-0.27 \pm 0.06\text{‰}$ and $-0.82 \pm 0.07\text{‰}$. The heaviest $\delta^{66}\text{Zn}$ value corresponds to the UB fraction; the lightest, the M4 fraction. These values also display a general trend of isotopic lightening throughout the distinct matrices (Fig. 5c), except for the M1 value of $-0.60 \pm 0.03\text{‰}$ being heavier than the M2 value of $-0.45 \pm 0.06\text{‰}$. Figure 3d shows the $\delta^{56}\text{Fe}$ and $\delta^{66}\text{Zn}$ values compared to one another. There is a clear bi-modal distribution here, with UB through M3 clustered together and M4 distinctly lighter in both the Fe and Zn systems. Figure 5a-c displays iron and zinc isotope data in order of deformation events, as interpreted through structural relationships between matrix generations (Angiboust et al., 2014; Locatelli et al., 2018, 2019a). The exception to this chronological ordering is the point representing blueschist overprinting, circled in blue in figures displaying whole-rock data (Fig. 5a, c, d).

5.3 Sm-Nd Garnet Geochronology Results

Fig. 6 shows the isochrons calculated with the whole-rock, five leachates, and two residue fractions, whilst Table 2b shows measured Sm-Nd ratios and errors. Age error is reported as the 2σ confidence interval of repeat analysis of each sample for isochrons with good fit ($\rho > 0.05$) and 2σ multiplied by the square root of the MSWD for isochrons with poor fit ($\rho < 0.05$). All isochrons were calculated using IsoplotR (Vermeesch, 2018). The eight point isochron, shown in Fig. 6a, which includes the whole-rock, all five leachates, and both residues, yields an age of 38.42 ± 7.13 Ma. The two residue points introduce a large amount of scatter, resulting in an extremely high MSWD of 230. The powder residue, which plots above the isochron, may have included older zircons (Rubatto and Hermann, 2003), which have a high Sm/Nd ratio and

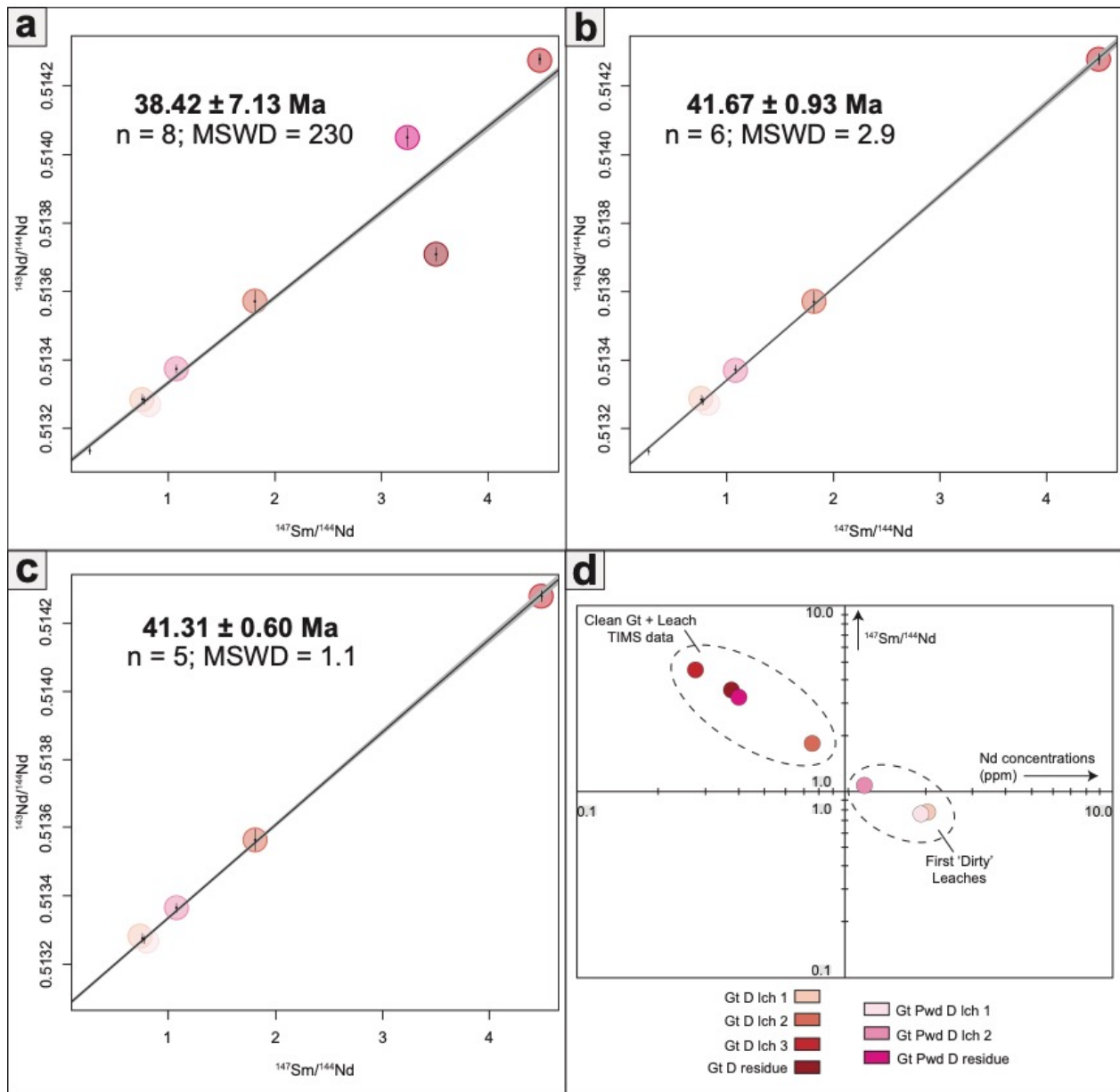


Fig. 6. Isochrons used to determine the age of garnet crystallization in the metasomatic rinds from the Monviso Ophiolite. (a) An eight-point isochron that results in a geologically improbable age and large MSWD. This isochron includes one whole-rock point, five leachates, and two residues. (b) A six-point isochron that excludes the two residue points that introduce significant amounts of scatter. (c) The five-point isochron that excludes the whole-rock point, resulting in an internal isochron. (d) Plot comparing Nd concentration to $^{147}\text{Sm}/^{144}\text{Nd}$ ratio, analyzing the cleanliness of each leachate and residue point included on the isochrons; after Star et al. (2020). Unusually, the third leachate is cleaner than both residue points.

are resistant to dissolution (Baxter and Caddick., 2017). The dissolution of zircons during full dissolution of the residue, but not during the previous partial dissolution stages, may be explained by the much higher concentrations of HF used during this process. The garnet residue, however, plots below the isochron for unclear reasons, presumably incorporating another restitic phase, younger than the garnet, that has resisted partial dissolution. As these rocks contain significant proportions of rutile, this mineral phase may be the culprit. A two point isochron between the whole-rock and garnet residue point yields an age of 27.30 ± 0.87 Ma, which is highly geologically improbable for this locality based on extensive structural and geochronological studies (Duchêne et al., 1997; Rubatto and Hermann, 2003; Rubatto and Angiboust, 2015; Garber et al., 2020; Agard and Handy, 2021). For these reasons this study excludes these two points to create a six-point isochron (Fig. 6b) that yields an age of 41.67 ± 0.93 Ma. The most significant source of scatter on this isochron originates from the whole-rock point, resulting in an MSWD of 2.9. One explanation for the origin of this scatter is minor isotopic disequilibrium between the rock matrix and the garnet which represents a very feasible possibility given the metasomatic origin of the sample. Without the whole-rock anchor point, the five point internal isochron (Fig. 6c) yields an age of 41.31 ± 0.60 Ma with an MSWD of 1.1. We choose to present the 5-point isochron age of 41.31 ± 0.60 Ma (excluding the whole rock) as the timing of M4 formation, while noting that the five and six point isochrons yield similar enough ages within error for the choice to be largely inconsequential for the purposes of this study.

6. Discussion

In the following discussion, we address several key questions: (1) what processes and fluid compositions are responsible for the isotopic changes seen in the Monviso eclogite

breccias; (2) where are the fluids sourced from and what are the implications for the redox-influencing potential of fluids produced from different sources; (3) what is the chronological history of subduction and exhumation for the Monviso Ophiolite and the duration of fluid flow and brecciation associated with the formation of the eclogite breccias.

6.1 Isotopic Compositions of Fluids in the Monviso Ophiolite

As discussed in sections 1 and 2, Fe and Zn isotope fractionation are expected to vary in response to fluid influx and outflux. The presence of species such as sulfate or carbonate within incoming or outgoing fluids is expected to impact both iron and zinc isotopes, while the difference in Fe²⁺ and Fe³⁺ fluid mobility only facilitates iron isotope fractionation. A previous study found that garnet crystals recorded heavier iron isotopes from core to rim suggest that the residual rock became isotopically heavier as a result of progressive subduction and dehydration (Gerrits et al., 2019). These observations imply that the fluids resulting from dehydration reactions preferably incorporate light iron isotopes (Gerrits et al., 2019). Additionally, sulfate and carbonate complexes have been suggested to preferentially incorporate isotopically heavy Zn (Black et al., 2011) especially during prograde metamorphism (Pons et al., 2016), leaving behind progressively lighter $\delta^{66}\text{Zn}$ values in serpentinite assemblages as P-T conditions increase.

Considering these different controls on Fe and Zn isotopic fractionation, four main hypotheses based on the different possible co-variations are suggested in Fig. 1.

The iron and zinc isotopic compositions of the whole-rock fractions display a four distinct changes (Fig. 7): (1) a negative correlation from UB to M1, (2) a negative correlation in the opposite direction from M1 to M2, (3) no change in Fe but lightening of Zn from M2 to M3, and (4) a positive correlation from M3 to M4. Fe isotopes become heavier between UB and M1, lighten marginally between M1 and M2/M3, and then lighten significantly from M2/M3 to M4.

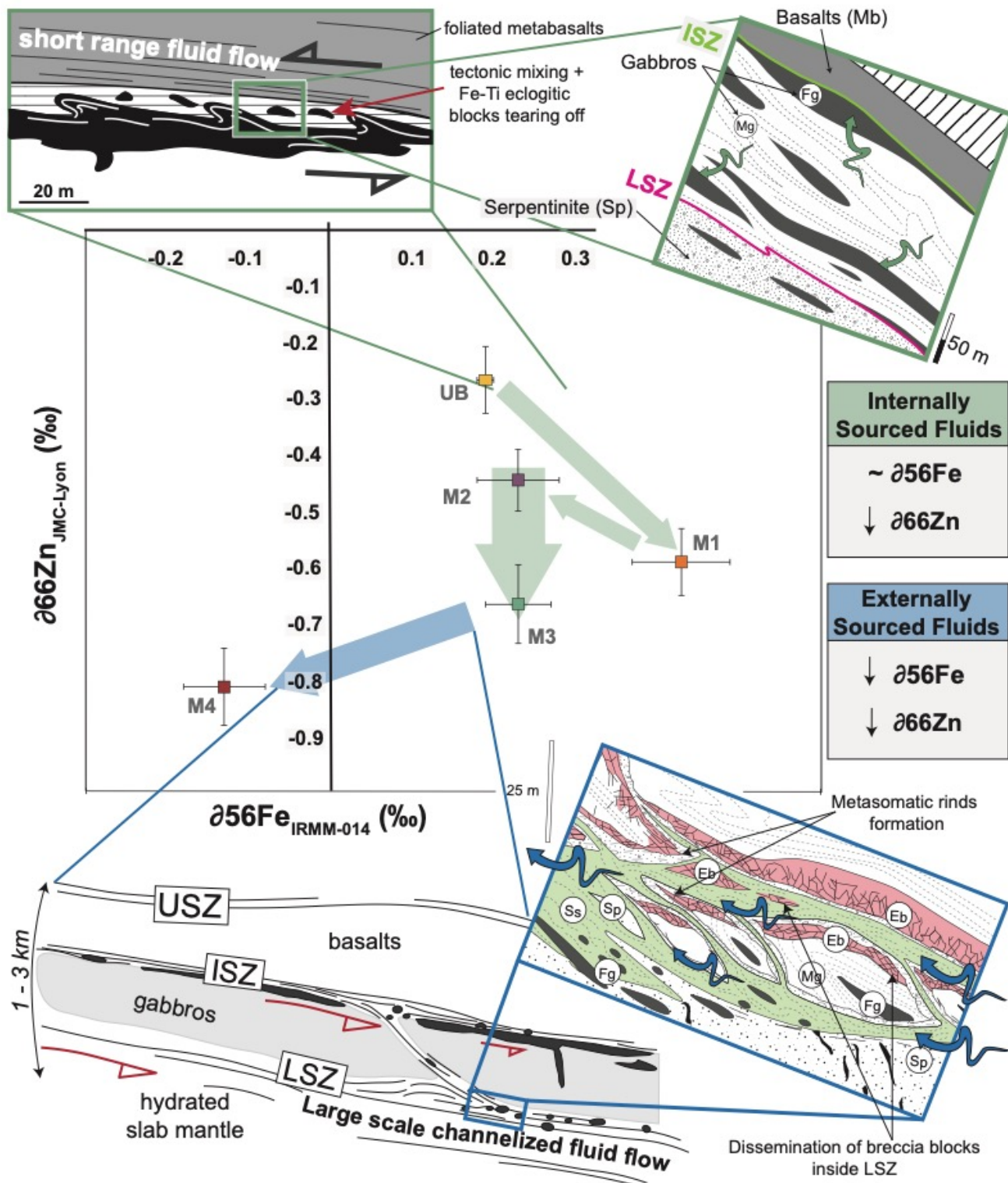


Fig. 7. Iron and zinc isotopic variations, with graphical representations of fluid movement and subsequent matrix crystallization that likely influenced the measured fractionation; after Angiboust et al. (2011) and Locatelli et al. (2019b).

With the exception of M1, the zinc isotopes display a general lightening trend throughout the crystallization of matrix generations (UB, M2, and M3), while the iron isotopes remain relatively unchanged. Between UB and M1, the Fe isotopes become heavier and the Zn isotopes become lighter. Conversely, from M1 to M2, the opposite happens: Fe isotopes get lighter and Zn isotopes get heavier. The Fe isotopic signature of the M4 whole-rock is significantly lighter than the other matrix generations presented in this study (Fig. 7).

The first two negative correlations from UB to M1 and M1 to M2 best fit with hypothesis 4 (Fig. 1d) where fluids with isotopically heavier Zn and lighter Fe than their source move into or out of the system. M1 displays heavier Fe and lighter Zn isotopes than UB, suggesting that fluids fractionated light Fe and heavy Zn away from the M1 matrix, perhaps during initial crystallization or during blueschist retrogression. From M1 to M2, we see light Zn and heavy Fe, signaling the influx of these sulfate- and/or carbonate-rich fluids. Previous studies suggest that sulfate-bearing fluids preferentially incorporate heavy Zn isotopes thus leaving behind a progressively lighter Zn isotopic reservoir to be tapped as dehydration proceeds (Pons et al., 2016). Thus we interpret the lightening in fluid-sourced Zn isotopes to reflect progressive lightening of that fluid source.

M2 and M3 display a lightening of Zn isotopes with no change in Fe isotopes, consistent with hypothesis 2 (Fig. 1b). As there are orders of magnitude less zinc than iron present in the system, bulk zinc isotopic values are likely easier to influence as dehydration proceeds. This difference in the iron and zinc systems could signify a volume of sulfate-bearing fluids that is significant enough to modify zinc isotopes, but not enough to influence iron isotopic change. Another possibility is the presence of some species or complex that influences zinc fractionation but not iron. The intermediate negative fractionation effect in zinc could suggest the presence of

sulfides rather than sulfates in the fluids, which would leave the iron isotopes relatively unchanged (Inglis and Moynier, 2021). The abrupt change in Fe isotopes from M1 to M2, then the consistency in Fe isotopes from M2 to M3, could also suggest a change in the source of the fluids between M1 and M2.

The trend of lightening iron and zinc isotopes from M3 to the metasomatic rind (M4) indicates a positive correlation between the iron and zinc systems (Fig. 7) consistent with hypothesis 3 (Fig. 1c) with respect to M4 crystallization. The change in iron isotope values is significantly larger in magnitude not only with respect to values presented in this study, but also in comparison to other studies of iron isotopic behavior at high temperatures (Dauphas et al., 2009, 2014; Debret et al., 2016, 2018; Inglis et al., 2017; Gerrits et al., 2019). This significant lightening of iron isotopes is accompanied by a continuation of the progressively lightening trend previously observed in the zinc isotopes between M2 and M3. The influx of incoming fluids with an isotopically light iron signature is sufficient to cause this major change in the iron isotope system. The lightening in both iron and zinc isotope systems likely signifies the presence of sulfate and carbonate complexes within the fluid. In Gerrits et al. (2019), the high pressure garnets display progressively heavier iron isotopes from core to rim while the f_{O_2} gets more reduced. This data is interpreted as the residual garnet getting heavier due to the release of oxidizing, isotopically light fluids. In this study, the M4 whole rock point shows the opposite pattern – it gets isotopically lighter as a result of recrystallization. Our interpretation is that these eclogite breccias are generally influenced by the effects of fluid influx rather than dehydration and the loss of fluids. As a result the crystallization of M4 experiences the effects of the influx of isotopically light fluids that were predicted to have been produced due to dehydration of external

sources in Gerrits et al. (2019). The continued lightening of Zn isotopes in M4 is consistent with a progressively lightening external fluid source.

Figure 5a-c displays iron and zinc isotope data in order of deformation events, as interpreted through structural relationships between matrix generations (Angiboust et al., 2014; Locatelli et al., 2018, 2019a). Figure 5a and c also shows the Fe and Zn isotopic values of a section of M1 matrix that was largely overprinted later by blueschist facies assemblages, circled in blue in figures displaying whole-rock data (Fig. 5a, c, d). This data point was largely analyzed to test if late-stage retrogression that resulted in glaucophane crystallization had an overarching effect on pre-existing matrix generations. The isotopic data for the retrogression is similar but slightly lighter Fe and heavier Zn than the host M1 matrix for both Fe and Zn, as shown in Figure 5d. This change suggests that fluids enriched in comparatively isotopically light Fe and heavy Zn also had some influence on crystallization associated with blueschist retrogression. The blueschist sample analyzed, however, was primarily glaucophane, which raises the question of Fe and Zn isotope fractionation between different mineral phases.

In contrast to the whole rock values, the garnet fractions analyzed in this study (Fig. 5b) display no obvious interpretable pattern. Fe isotope fractionation between different mineral phases is not well understood, especially in open, metasomatic systems. Garnet is also a relatively minor phase in these eclogite breccias and the amount of garnet varies considerably between different matrix generations. Therefore, the changes in the Fe values in the garnet fractions is likely also controlled by the poorly constrained mineral fractionation factors in addition to system-scale factors and thus the whole rock analyses were deemed to be a more useful reflection of the overall changes happening in the system, especially those involving open system fluid processes.

6.2 Fluid Sources and Implications for Redox Processes

The eclogite breccias crystallized during the delamination and exhumation of the ISZ and LSZ. This process began with the mylonitization of Fe-Ti metagabbro blocks within the ISZ. Repeated fracturing processes associated with the mylonitization of the shear zone, in conjunction with dehydration reactions, resulted in locally derived, short range fluid flow (Angiboust et al., 2011). The crystallization of distinct matrix generations began with the omphacite-rich M1 matrix. Geochemical patterns of M1, both the wide compositional ranges and major and trace element similarities to metagabbros from the ISZ, suggest that M1 omphacites crystallized in the presence of fluids that originated from Mg-Al metagabbros in the ISZ (Locatelli et al., 2019b). Pseudosection modelling ascribes M1 crystallization with peak burial conditions, and Mg-Al metagabbros within the ISZ still contain hydrated phases at peak P-T conditions as opposed to Fe-Ti metagabbros. M2 major and trace element concentrations are similar to M1, with the exception of Cr enrichment (Locatelli et al., 2019b). This enrichment suggests a mixed fluid source, with at least a small amount of fluids resulting from the brucite-out dehydration reaction occurring in the serpentinite sole. The trace element trends and compositions of the M3 matrix are markedly distinct from neighboring Mg-Al and Fe-Ti metagabbros, particularly with respect to strong Cr, Ni, and Co enrichments, which approach serpentinite concentrations (Locatelli et al., 2019b). The M3 matrix crystallization occurred on the retrograde path, and marks the beginning of fluid emplacement from antigorite-out serpentinite dehydration in deeper portions of the subducting slab. The metasomatic rinds (M4) that rim brecciated blocks disseminated within the LSZ are enriched in Mg, Cr, and Ni, which were apparently introduced by hydrous fluid infiltration (Angiboust et al., 2014). The M4 matrix is strongly metasomatized, and signifies the establishment of long-lived fluid-focusing structures

that carried fluids from deep oceanic slab serpentinites to the subduction interface. Angiboust et al. (2014) suggests that fluid infiltration occurred in pulses, with the event that facilitated rind crystallization being the volumetrically largest fluid migration event.

The iron and zinc isotope data presented in this study is consistent with a hypothesis in which fluids that facilitated M1 and M2 were predominantly locally sourced, existed in small amounts, and infiltrated from the Mg-Al metagabbros to the Fe-Ti metagabbros (Locatelli et al., 2019b) through small, transient conduits (Fig. 7). M1 is clearly distinct from M2 and M3, likely due to a different fluid source (hydrated phases in the Mg-Al metagabbros compared to serpentinite-derived fluids). M3 experienced an intermediate amount of externally derived fluids that remained localized to breccia formation. The progressively decreasing $\delta^{66}\text{Zn}$ values in M2 through M4 suggest that oxidizing species, such as sulfate, carbonate, or perhaps sulfide, were present to some degree in these locally derived fluids capable of mobilizing and fractionating Zn isotopes. The iron isotopes remain relatively unchanged in M2 and M3, perhaps due to the fluid/rock ratios during M2-M3 fluid influx, making them unable to measurably influence the bulk isotope values of iron in these Fe-enriched rocks. The small, transient conduits facilitating the early movement of externally-derived fluids were also likely insufficient to affect the difference in iron fluid mobility between Fe^{2+} and Fe^{3+} .

The decrease in zinc isotopes from M2 to M4 is gradual overall, while the iron isotopes are heavier in M1 and display an abrupt lightening in M4. The iron and zinc isotopic data, in conjunction with other geochemical data (Angiboust et al., 2014; Locatelli et al., 2019b), presents compelling evidence that the metasomatic rind was a consequence of an externally derived fluid that is distinct from the earlier matrix generations (Fig. 7). Angiboust et al. (2011) noted the observation that the Fe-Ti metagabbros that act as the protolith for the breccias likely

originated in the ISZ, although they are observed in present day embedded within the antigorite schists of the LSZ. They hypothesize that a longer-lived pervasive deformation-enhanced fluid pathway at the gabbro-serpentinite boundary resulted in the observed strong metasomatism, mechanical weakening, and dismembering of block fragments within the LSZ (Angiboust et al., 2011). Through LA-ICP-MS trace element analysis of LSZ eclogites, Angiboust et al. (2014) suggests that this external fluid was derived from the serpentinite sole below the LSZ. The considerable lightening of both $\delta^{66}\text{Zn}$ and $\delta^{56}\text{Fe}$ values in M4 suggests the movement of external fluids (Fujii et al., 2011) concentrated in sulfate ions (Pons et al., 2011) through the downgoing mantle and crust. As shown by Pons et al. (2016), zinc isotopic values within subducted serpentinites get progressively lighter as metamorphic grade increases. The values in this study are significantly lighter than those reported by Pons et al. (2016). Perhaps the fluids moving through the Monviso Ophiolite are flushing sulfate ions from the system, therefore removing heavy Zn isotopes from the matrix generations and leaving behind negative Zn isotopes in the whole rocks. Our interpretation, however, is that the serpentinite sole experienced dehydration reactions prior to the ones that influenced M4 crystallization, resulting in a lighter bulk Zn isotopic signature in the serpentinite sole. While the fluids resulting from the dehydration reactions that occurred during retrogression likely contained heavier Zn than the serpentinite sole, these Zn isotopes were lighter than the eclogite breccias in this study. The significant amount of externally derived fluids also prove to be sufficient to affect the oxidation state of iron, making isotopically light, fluid-mobile Fe^{2+} available for metasomatic rind crystallization. The presence of isotopically light Fe suggests that the fluids are transporting light isotopes, which might seem at odds with the hypothesis that sulfate complexes present in the fluids would transport heavy Zn isotopes.

The iron and zinc isotopic values from these metagabbro brecciated blocks embedded within the LSZ confirm previous observations that early matrix crystallization (M1-2) began with small-scale internally derived fluids, and M3 experienced small amounts of external fluid emplacement that stayed localized to the breccias. Additionally, these data enforce that rind formation (M4) that corresponds with shear motion and exhumation (see section 6.3) was facilitated or assisted by large-scale externally derived fluids. These externally derived fluids, likely originating from the serpentinite sole below the LSZ, clearly have a significant effect on the isotopic composition and redox state of the lithologies they encounter. Because these fluids move through a large-scale, long-lasting conduit created by shear motion and rheological differences (Angiboust et al., 2011, 2014; Locatelli et al., 2019b), they likely continued to move upward, into the mantle wedge above the subduction interface. The presence of these externally-derived fluids, and data to support the effect they have on redox conditions of mineral crystallization, provide a cause to the observed effect of mantle wedge oxidation (Carmichael, 1991; Behrens and Gaillard, 2006; Kelley and Cottrell, 2009; Brounce et al., 2014).

6.3 Timescales of Fluid and Deformation Processes

The age of the metasomatic rinds determined in this study is consistent with previous geochronological studies of the Lago Superiore Unit, which predominantly focus on the timing of prograde and peak metamorphism (Fig. 8a). An age of 49 Ma from a mafic eclogite (Duchêne et al., 1997) results from Lu-Hf garnet geochronology, which generally serves to report early

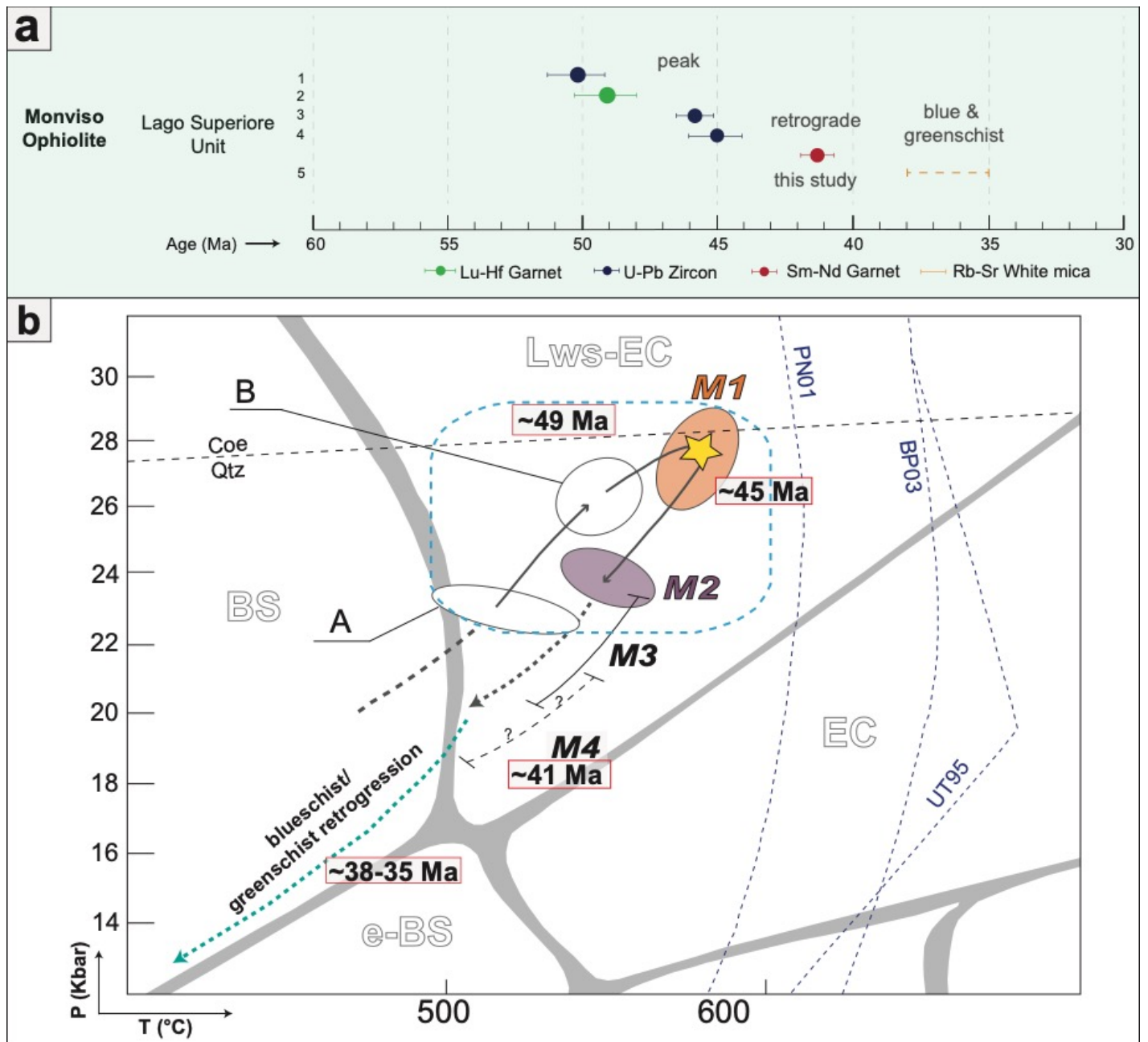


Fig. 8. A complication of previously published age data, this study's Sm-Nd bulk garnet age, and the pressure-temperature-time path of the Monviso ophiolite. (a) The prograde, peak, retrograde, and blueschist/greenschist ages of the Monviso ophiolite sequence as determined by a Lu-Hf garnet age, U-Pb zircon ages, Sm-Nd bulk garnet age, and Rb-Sr white mica ages; after Star et al. (2020). (b) A sketch of the P-T path of the Monviso ophiolite, with approximate ages included. The M4 and blueschist/greenschist paths are approximations based on previous studies; after Locatelli et al. (2018). In figure citations: (1) Garber et al. (2020); (2) Duchêne et al. (1997); (3) Rubatto and Hermann (2003); (4) Rubatto and Angiboust (2015); (5) Angiboust and Glodney (2020).

garnet growth within the system and thus likely dates prograde metamorphism (Kohn, 2009; Baxter and Scherer, 2013). Two U-Pb ages around ~45-46 Ma (Rubatto and Hermann, 2003; Rubatto and Angiboust, 2015) have generally been interpreted to correspond to the timing of peak metamorphism and also to the onset of small-scale brecciation, likely facilitated by small-scale, short-range fluid flow derived from local dehydration reactions. An earlier age of ~50 Ma interpreted to reflect peak metamorphism (Garber et al., 2020) is a U-Pb zircon age of localities located further south than the brecciated blocks presented in this study. It is unclear whether differences in these U-Pb ages reflect real variations in peak burial age across the Monviso area or methodological errors (Garber et al., 2020). The blue- and greenschist-facies age range of 38-35 Ma represents a series of Rb-Sr mixed white mica ages (Angiboust and Glodny, 2020). These ages are reported as a range because of the overprinted nature of the white mica crystals analyzed and records a contemporaneous re-equilibration that occurred in major shear zones during the latter stages of exhumation.

The age of 41.31 ± 0.60 Ma for the M4 sample is consistent with fluid influx and M4 recrystallization occurring along the retrograde path between peak metamorphism and later blueschist/greenschist overprinting (Fig. 8b). Comparing the approximate timing of peak metamorphism (~46-45 Ma) with this new age constrains results place a ~4 Ma time period between peak burial and the large scale fluid ingress associated with metasomatic rind formation (Fig. 8b). Given the typically rapid timescales of subduction and exhumation, this time gap is quite substantial and could signify that the Monviso Ophiolite is exhuming relatively slowly, or that they remained at high pressure conditions for quite some time.

7. Conclusions

The iron and zinc isotopes covary and convey the presence of at least two crystallization events that are mediated by distinct fluids. The crystallization of the M1 matrix coincides with peak burial conditions and dehydration reactions within metagabbro lithologies. The other matrices within eclogite-breccia blocks – M2 and M3 – were likely influenced by a mixture of internally and externally sourced fluids that did not have a drastic effect on iron isotopes, but imparted an intermediate negative isotope effect on $\delta^{66}\text{Zn}$. The crystallization of the metasomatic rind imparted a negative isotope effect on both iron and zinc systems, implying an externally sourced, isotopically light fluid compared to its source that is sulfate- and carbonate-rich moving through the mafic slab and removing oxidized iron. This removal suggests that isotopically light fluid that has an effect on redox state moved through the LSZ via long-lived high-strain channels and into lithologies situated above the subduction interface, such as the mantle wedge. This data also has implications for the future use of iron and zinc isotopes to study the composition of deep-earth fluids and the effect these fluids have on the redox state of the mantle and arc volcanism.

The determined garnet bulk age of the metasomatic rind garnets is 41.31 ± 0.60 Ma. This age is consistent with previous geochronological studies and places M1-4 crystallization occurring on the retrograde metamorphism path during a period of ~ 4 Ma. The dis-equilibrium between the whole rock and garnets, shown by the slight discrepancy in ages between the 5- and 6-point isochrons, strengthens the hypothesis that M4 crystallization occurred during an open-system metasomatic event.

References

- Agard, P., 2021, Subduction of oceanic lithosphere in the Alps: Selective and archetypal from (slow-spreading) oceans: *Earth-Science Reviews*, v. 214, p. 103517, doi:10.1016/j.earscirev.2021.103517.
- Agard, P., and Handy, M.R., 2021, Ocean Subduction Dynamics in the Alps: *Elements*, v. 17, p. 9–16, doi:10.2138/gselements.17.1.9.
- Agard, P., Yamato, P., Jolivet, L., and Burov, E., 2009, Exhumation of oceanic blueschists and eclogites in subduction zones: Timing and mechanisms: *Earth-Science Reviews*, v. 92, p. 53–79, doi:10.1016/j.earscirev.2008.11.002.
- Angiboust, S., Agard, P., Raimbourg, H., Yamato, P., and Huet, B., 2011, Subduction interface processes recorded by eclogite-facies shear zones (Monviso, W. Alps): *Lithos*, v. 127, p. 222–238, doi:10.1016/j.lithos.2011.09.004.
- Angiboust, S., Agard, P., Yamato, P., and Raimbourg, H., 2012, Eclogite breccias in a subducted ophiolite: A record of intermediatedepth earthquakes? *Geology*, v. 40, p. 707–710, doi:10.1130/G32925.1.
- Angiboust, S., and Glodny, J., 2020, Exhumation of eclogitic ophiolitic nappes in the W. Alps: New age data and implications for crustal wedge dynamics: *Lithos*, v. 356–357, doi:10.1016/j.lithos.2020.105374.
- Angiboust, S., Pettke, T., De Hoog, J.C.M., Caron, B., and Oncken, O., 2014, Channelized fluid flow and eclogite-facies metasomatism along the subduction shear zone: *Journal of Petrology*, v. 55, p. 883–916, doi:10.1093/petrology/egu010.
- Baxter, E.F., and Caddick, M.J., 2013, Garnet growth as a proxy for progressive subduction zone dehydration: *Geology*, v. 41, p. 643–646, doi:10.1130/G34004.1.

- Baxter, E.F., Caddick, M.J., and Dragovic, B., 2017, Garnet: A Rock-Forming Mineral Petrochronometer: *Reviews in Mineralogy and Geochemistry*, v. 83, p. 469–533, doi:10.2138/rmg.2017.83.15.
- Baxter, E.F., and Scherer, E.E., 2013, Garnet geochronology: Timekeeper of tectonometamorphic processes: *Elements*, v. 9, p. 433–438, doi:10.2113/gselements.9.6.433.
- Behrens, H., and Gaillard, F., 2006, Geochemical aspects of melts: Volatiles and redox behavior: *Elements*, v. 2, p. 275–280, doi:10.2113/gselements.2.5.275.
- Black, J.R., Kavner, A., and Schauble, E.A., 2011, Calculation of equilibrium stable isotope partition function ratios for aqueous zinc complexes and metallic zinc: *Geochimica et Cosmochimica Acta*, v. 75, p. 769–783, doi:10.1016/j.gca.2010.11.019.
- Brace, W.F., 1984, Permeability of crystalline rocks: New in situ measurements: *Journal of geophysical research*, v. 89, p. 4327–4330.
- Broadwell, K.S., Locatelli, M., Verlaguet, A., Agard, P., and Caddick, M.J., 2019, Transient and periodic brittle deformation of eclogites during intermediate-depth subduction: *Earth and Planetary Science Letters*, v. 521, p. 91–102, doi:10.1016/j.epsl.2019.06.008.
- Brounce, M.N., Kelley, K.A., and Cottrell, E., 2014, Variations in Fe³⁺/PFe of Mariana Arc Basalts and Mantle Wedge fO₂: *Journal of Petrology*, v. 55, p. 2514–2536, doi:10.1093/petrology/egu065.
- Carmichael, I.S. (1991) The Redox States of Basic and Silicic Magmas: A Reflection of Their Source Regions? *Contributions to Mineralogy and Petrology*, 106, 129-141.
<http://dx.doi.org/10.1007/BF00306429>
- Chiaradia, M., 2021, Zinc systematics quantify crustal thickness control on fractionating

- assemblages of arc magmas: *Scientific Reports*, v. 11, p. 1–14, doi:10.1038/s41598-021-94290-6.
- Codillo, E.A., Le Roux, V., and Marschall, H.R., 2018, Arc-like magmas generated by mélange-peridotite interaction in the mantle wedge: *Nature Communications*, v. 9, doi:10.1038/s41467-018-05313-2.
- Dauphas, N. et al., 2014, Magma redox and structural controls on iron isotope variations in Earth's mantle and crust: *Earth and Planetary Science Letters*, v. 398, p. 127–140, doi:10.1016/j.epsl.2014.04.033.
- Dauphas, N., Craddock, P.R., Asimow, P.D., Bennett, V.C., Nutman, A.P., and Ohnenstetter, D., 2009, Iron isotopes may reveal the redox conditions of mantle melting from Archean to Present: *Earth and Planetary Science Letters*, v. 288, p. 255–267, doi:10.1016/j.epsl.2009.09.029.
- Debret, B., Bouilhol, P., Pons, M.L., and Williams, H., 2018, Carbonate transfer during the onset of slab devolatilization: New insights from Fe and Zn stable isotopes: *Journal of Petrology*, v. 59, p. 1145–1166, doi:10.1093/petrology/egy057.
- Debret, B., Garrido, C.J., Pons, M.L., Bouilhol, P., Inglis, E., López Sánchez-Vizcaíno, V., and Williams, H., 2021, Iron and zinc stable isotope evidence for open-system high-pressure dehydration of antigorite serpentinite in subduction zones: *Geochimica et Cosmochimica Acta*, v. 296, p. 210–225, doi:10.1016/j.gca.2020.12.001.
- Debret, B., Millet, M.A., Pons, M.L., Bouilhol, P., Inglis, E., and Williams, H., 2016, Isotopic evidence for iron mobility during subduction: *Geology*, v. 44, p. 215–218, doi:10.1130/G37565.1.
- Duchêne, S., Blichert-Toft, B., Luais, B., Télouk, P., Lardeaux, J.-M., and Albarède, F., 1997,

The Lu Hf dating of garnets and the ages of the Alpine high-pressure metamorphism

Related papers: *Nature*, v. 387, p. 585–589.

Evans, K.A., 2012, The redox budget of subduction zones: *Earth-Science Reviews*, v. 113, p. 11–32, doi:10.1016/j.earscirev.2012.03.003.

Evans, K.A., and Powell, R., 2015, The effect of subduction on the sulphur, carbon and redox budget of lithospheric mantle: *Journal of Metamorphic Geology*, v. 33, p. 649–670, doi:10.1111/jmg.12140.

Fujii, T., Moynier, F., Pons, M.L., and Albarède, F., 2011, The origin of Zn isotope fractionation in sulfides: *Geochimica et Cosmochimica Acta*, v. 75, p. 7632–7643, doi:10.1016/j.gca.2011.09.036.

Fujii, T., Moynier, F., Telouk, P., and Abe, M., 2010, Experimental and theoretical investigation of isotope fractionation of zinc between aqua, chloro, and macrocyclic complexes: *Journal of Physical Chemistry A*, v. 114, p. 2543–2552, doi:10.1021/jp908642f.

Fumagalli, P., and Poli, S., 2005, Experimentally determined phase relations in hydrous peridotites to 6.5 GPa and their consequences on the dynamics of subduction zones: *Journal of Petrology*, v. 46, p. 555–578, doi:10.1093/petrology/egh088.

Gaborieau, M., Laubier, M., Bolfan-Casanova, N., McCammon, C.A., Vantelon, D., Chumakov, A.I., Schiavi, F., Neuville, D.R., and Venugopal, S., 2020, Determination of Fe³⁺/ΣFe of olivine-hosted melt inclusions using Mössbauer and XANES spectroscopy: *Chemical Geology*, v. 547, p. 119646, doi:10.1016/j.chemgeo.2020.119646.

Garber, J.M., Smye, A.J., Feineman, M.D., Kylander-Clark, A.R.C., and Matthews, S., 2020, Decoupling of zircon U–Pb and trace-element systematics driven by U diffusion in eclogite-facies zircon (Monviso meta-ophiolite, W. Alps): *Contributions to Mineralogy and*

- Petrology, v. 175, p. 1–25, doi:10.1007/s00410-020-01692-2.
- Gerrits, A.R., Inglis, E.C., Dragovic, B., Starr, P.G., Baxter, E.F., and Burton, K.W., 2019, Release of oxidizing fluids in subduction zones recorded by iron isotope zonation in garnet: *Nature Geoscience*, v. 12, p. 1029–1033, doi:10.1038/s41561-019-0471-y.
- Gilio, M., Scambelluri, M., Agostini, S., Godard, M., Pettke, T., Agard, P., Locatelli, M., and Angiboust, S., 2020, Fingerprinting and relocating tectonic slices along the plate interface: Evidence from the Lago Superiore unit at Monviso (Western Alps): *Lithos*, v. 352–353, p. 105308, doi:10.1016/j.lithos.2019.105308.
- Glodny, J., Austrheim, H., Molina, J.F., Rusin, A.I., and Seward, D., 2003, Rb/Sr record of fluid-rock interaction in eclogites: The Marun-Keu complex, Polar Urals, Russia: *Geochimica et Cosmochimica Acta*, v. 67, p. 4353–4371, doi:10.1016/S0016-7037(03)00370-3.
- Hacker, B.R., 2008, H₂O subduction beyond arcs: *Geochemistry, Geophysics, Geosystems*, v. 9, doi:10.1029/2007GC001707.
- Hacker, B.R., Peacock, S.M., Abers, G.A., and Holloway, S.D., 2003, Subduction factory 2. Are intermediate-depth earthquakes in subducting slabs linked to metamorphic dehydration reactions? *Journal of Geophysical Research: Solid Earth*, v. 108, doi:10.1029/2001jb001129.
- Harvey, J., and Baxter, E.F., 2009, An improved method for TIMS high precision neodymium isotope analysis of very small aliquots (1–10 ng): *Chemical Geology*, v. 258, p. 251–257, doi:10.1016/j.chemgeo.2008.10.024.
- Hermann, J., Spandler, C., Hack, A., and Korsakov, A. V., 2006, Aqueous fluids and hydrous melts in high-pressure and ultra-high pressure rocks: Implications for element transfer in subduction zones: *Lithos*, v. 92, p. 399–417, doi:10.1016/j.lithos.2006.03.055.

- Inglis, E.C. et al., 2017, The behavior of iron and zinc stable isotopes accompanying the subduction of mafic oceanic crust: A case study from Western Alpine ophiolites: *Geochemistry, Geophysics, Geosystems*, v. 18, p. 2562–2579, doi:10.1002/2016GC006735.Received.
- Inglis, E.C, and Moynier, F., 2021, Zinc and Copper Isotopes as Tracers of Redox Processes *in* Moretti, R., and Neuville, D., 2021, *Magma Redox Geochemistry* (R. Moretti & D. R. Neuville, Eds.): American Geophysical Union, p. 331-344, doi:10.1002/9781119473206.
- van Keken, P.E., Hacker, B.R., Syracuse, E.M., and Abers, G.A., 2011, Subduction factory: 4. Depth-dependent flux of H₂O from subducting slabs worldwide: *Journal of Geophysical Research: Solid Earth*, v. 116, doi:10.1029/2010JB007922.
- Kelley, K.A., and Cottrell, E., 2012, The influence of magmatic differentiation on the oxidation state of Fe in a basaltic arc magma: *Earth and Planetary Science Letters*, v. 329–330, p. 109–121, doi:10.1016/j.epsl.2012.02.010.
- Kelley, K.A., and Cottrell, E., 2009, Water and the oxidation state of subduction zone magmas: *Science*, v. 325, p. 605–607, doi:10.1126/science.1174156.
- Kohn, M.J., 2009, Models of garnet differential geochronology: *Geochimica et Cosmochimica Acta*, v. 73, p. 170–182, doi:10.1016/j.gca.2008.10.004.
- Konrad-Schmolke, M., O’Brien, P.J., and Zack, T., 2011, Fluid migration above a subducted slab-constraints on amount, pathways and major element mobility from partially overprinted eclogite-facies rocks (Sesia Zone, Western Alps): *Journal of Petrology*, v. 52, p. 457–486, doi:10.1093/petrology/egq087.
- van Kooten, E., and Moynier, F., 2019, Zinc isotope analyses of singularly small samples (<5 ng Zn): Investigating chondrule-matrix complementarity in Leoville: *Geochimica et*

- Cosmochimica Acta, v. 261, p. 248–268, doi:10.1016/j.gca.2019.07.022.
- Kostenko, O., Jamtveit, B., Austrheim, H., Pollok, K., and Putnis, C., 2002, The mechanism of fluid infiltration in peridotites at Almklovdaalen, western Norway: *Geofluids*, v. 2, p. 203–215, doi:10.1046/j.1468-8123.2002.00038.x.
- Lee, C.T.A., Luffi, P., Le Roux, V., Dasgupta, R., Albarède, F., and Leeman, W.P., 2010, The redox state of arc mantle using Zn/Fe systematics: *Nature*, v. 468, p. 681–685, doi:10.1038/nature09617.
- Locatelli, M., Federico, L., Agard, P., and Verlaguet, A., 2019a, Geology of the southern Monviso metaophiolite complex (W-Alps, Italy): *Journal of Maps*, v. 15, p. 283–297, doi:10.1080/17445647.2019.1592030.
- Locatelli, M., Verlaguet, A., Agard, P., Federico, L., and Angiboust, S., 2018, Intermediate-depth brecciation along the subduction plate interface (Monviso eclogite, W. Alps): *Lithos*, v. 320–321, p. 378–402, doi:10.1016/j.lithos.2018.09.028.
- Locatelli, M., Verlaguet, A., Agard, P., Pettke, T., and Federico, L., 2019b, Fluid Pulses During Stepwise Brecciation at Intermediate Subduction Depths (Monviso Eclogites, W. Alps): First Internally Then Externally Sourced: *Geochemistry, Geophysics, Geosystems*, v. 20, p. 5285–5318, doi:10.1029/2019GC008549.
- Marschall, H.R., and Schumacher, J.C., 2012, Arc magmas sourced from mélange diapirs in subduction zones: *Nature Geoscience*, v. 5, p. 862–867, doi:10.1038/ngeo1634.
- Mason, T.F.D., Weiss, D.J., Horstwood, M., Parrish, R.R., Russell, S.S., Mullane, E., and Coles, B.J., 2004, High-precision Cu and Zn isotope analysis by plasma source mass spectrometry part 1. Spectral interferences and their correction: *Journal of Analytical Atomic Spectrometry*, v. 19, p. 209–217, doi:10.1039/b306958c.

- Piccoli, F., Hermann, J., Pettke, T., Connolly, J.A.D., Kempf, E.D., and Vieira Duarte, J.F., 2019, Subducting serpentinites release reduced, not oxidized, aqueous fluids: *Scientific Reports*, v. 9, p. 1–7, doi:10.1038/s41598-019-55944-8.
- Pollington, A.D., and Baxter, E.F., 2011, High precision microsampling and preparation of zoned garnet porphyroblasts for Sm-Nd geochronology: *Chemical Geology*, v. 281, p. 270–282, doi:10.1016/j.chemgeo.2010.12.014.
- Pons, M.-L., Debret, B., Bouilhol, P., Delacour, A., and Williams, H., 2016, Zinc isotope evidence for sulfate-rich fluid transfer across subduction zones: *Nature Communications*, v. 7, doi:10.1038/ncomms13794.
- Pons, M.L., Quitté, G., Fujii, T., Rosing, M.T., Reynard, B., Moynier, F., Douchet, C., and Albarède, F., 2011, Early Archean serpentine mud volcanoes at Isua, Greenland, as a niche for early life: *Proceedings of the National Academy of Sciences of the United States of America*, v. 108, p. 17639–17643, doi:10.1073/pnas.1108061108.
- Rubatto, D., and Angiboust, S., 2015, Oxygen isotope record of oceanic and high-pressure metasomatism: a P–T–time–fluid path for the Monviso eclogites (Italy): *Contributions to Mineralogy and Petrology*, v. 170, p. 1–16, doi:10.1007/s00410-015-1198-4.
- Rubatto, D., and Hermann, J., 2003, Zircon formation during fluid circulation in eclogites (Monviso, Western Alps): Implications for Zr and Hf budget in subduction zones: *Geochimica et Cosmochimica Acta*, v. 67, p. 2173–2187, doi:10.1016/S0016-7037(02)01321-2.
- Rüpke, L.H., Morgan, J.P., Hort, M., and Connolly, J.A.D., 2004, Serpentine and the subduction zone water cycle: *Earth and Planetary Science Letters*, v. 223, p. 17–34, doi:10.1016/j.epsl.2004.04.018.

- Starr, P.G., Broadwell, K.S., Dragovic, B., Scambelluri, M., Haws, A.A., Caddick, M.J., Smye, A.J., and Baxter, E.F., 2020, The subduction and exhumation history of the Voltri Ophiolite, Italy: Evaluating exhumation mechanisms for high-pressure metamorphic massifs: *Lithos*, v. 376–377, p. 105767, doi:10.1016/j.lithos.2020.105767.
- Stern, R.J., 2002, Subduction zones: *Reviews of Geophysics*, v. 40, p. 3-1-3–38, doi:10.1029/2001RG000108.
- Sun, W., Arculus, R.J., Kamenetsky, V.S., and Binns, R.A. Release of gold-bearing fluids in convergent margin magmas prompted by magnetite crystallization: , p. 975–978.
- Vermeesch, P., 2018, IsoplotR: A free and open toolbox for geochronology: *Geoscience Frontiers*, v. 9, p. 1479–1493, doi:10.1016/j.gsf.2018.04.001.
- Williams, H.M., Nielsen, S.G., Renac, C., Griffin, W.L., O'Reilly, S.Y., McCammon, C.A., Pearson, N., Viljoen, F., Alt, J.C., and Halliday, A.N., 2009, Fractionation of oxygen and iron isotopes by partial melting processes: Implications for the interpretation of stable isotope signatures in mafic rocks: *Earth and Planetary Science Letters*, v. 283, p. 156–166, doi:10.1016/j.epsl.2009.04.011.
- Yamasaki, T., and Seno, T., 2003, Double seismic zone and dehydration embrittlement of the subducting slab: *Journal of Geophysical Research: Solid Earth*, v. 108, p. 1–21, doi:10.1029/2002jb001918.

SUPPLEMENTARY MATERIALS

M4 WR ALQ2 1.0 A spikesub BC Phoenix.xls

BOSTON COLLEGE PHOENIX

11-3-2017 version MJT

Full Sample Name: **Nd M4 WR ALQ2**
 Date of TIMS analysis: **4/13/22**
 estimated Nd load (ng): **4**

Position #: **8**

Rspike Values Nd {SmNd 1.0 A spike, 6-12-08 calib}						
142/144	143/144	145/144	146/144	148/144	150/144	[Nd150]
0.830433	0.494001	0.436936	0.885201	0.740574	198.371260	0.049114
						nm/g

Wt Sample (g)= **0.01325** g
 Wt Spike (g)= **0.3669** g

Mass Spectrometer Information:

Number of cycles measured:	136			
Number of cycles used:	125			
	start	average (from sheet)		
Filament Current range: from	3	3.1		Amps
Beam intensity range: from	0.546293311	1.257028759		Volts 144Nd.160
Temperature range: from	1500	1530		° C

Final Ratio Data:

Interference Values (oxide corrected; informational only... not used in this sheet)

Ce140/Nd144 **0.005351064**
 Pr141/Nd144 **0.00977179**
 Sm149/Nd144 **6.10487E-06**

for Ratios & %ISE: use grand mean oxygen corr, interference corr, exp normalized values

	142/144	143/144	145/144	146/144	148/144	150/144
Ratios	1.141807471	0.513153339	0.348441229	0.7219	0.241903506	0.381255515
%StdErr	0.000816785	0.000409497	0.000370752	0	0.000884881	0.000930113
<i>for comparison only</i>	142/144	143/144	145/144	146/144	148/144	150/144
DePaolo 88, p.14, ln. B'	1.141854	na	0.348416	0.721882	0.241572	na

FINAL DATA TO REPORT:

146/144 set to 0.7219

	142/144	143/144	145/144	146/144	148/144	150/144	150t/144s
Ratios	1.141844	0.513124	0.348405	0.721900	0.241618	0.236478	6.884984
± 2 S.E.	0.000019	0.000004	0.000003	0.000000	0.000004	0.000004	0.000128
				Epsilon143=	9.49	using (143/144)chur=	0.512638
				±	0.08	(Hamilton et al. 1983)	
<i>linked from Sm sheet</i>							
[Sm147]=	2.461044	nm/g	[Nd144]=	9.36351	nm/g		
±	0.000368		±	0.00169			
[Sm]=	2.467461	ppm	[Nd]=	5.67873	ppm		
±	0.000369		±	0.00103			
TOT ng Sm=	32.69385901		TOT ng Nd=	75.24320768			
		Sm147/Nd144=	0.262833				
		± 2 S.E.	0.000062				
		± 2RSE %	0%				

BOSTON COLLEGE PHOENIX

11-3-2017 version MJT

Full Sample Name: **M4 Gt D ALQ 1**
 Date of TIMS analysis: **6/14/22** Position #: **19**
 estimated Nd load (ng): **3.6**

Rspike Values Nd {SmNd 1.0 A spike, 6-12-08 calib}						
142/144	143/144	145/144	146/144	148/144	150/144	[Nd150]
0.830433	0.494001	0.436936	0.885201	0.740574	198.371260	0.049114
						nm/g

Wt Sample (g)= **0.0092525** g
 Wt Spike (g)= **0.18641** g

Mass Spectrometer Information:

Number of cycles measured:	130	
Number of cycles used:	117	
	start	average (from sheet)
Filament Current range: from	3.28	3.3
Beam intensity range: from	0.069212797	0.110107579
Temperature range: from	1507	1541
		Amps
		Volts 144Nd.160
		° C

Final Ratio Data:

Interference Values (oxide corrected; informational only... not used in this sheet)

Ce140/Nd144 **0.043626699**
 Pr141/Nd144 **0.018388665**
 Sm149/Nd144 **0.000547128**

for Ratios & %ISE: use grand mean oxygen corr, interference corr, exp normalized values

	142/144	143/144	145/144	146/144	148/144	150/144
Ratios	1.1415106	0.51401263	0.34878133	0.7219	0.24472886	1.802983
%StdErr	0.002965223	0.001601073	0.002391776	0	0.006775224	0.005266604
for comparison only	142/144	143/144	145/144	146/144	148/144	150/144
DePaolo 88, p.14, ln. B:	1.141854	na	0.348416	0.721882	0.241572	na

FINAL DATA TO REPORT:

146/144 set to 0.7219

	142/144	143/144	145/144	146/144	148/144	150/144	150t/144s
Ratios	1.141911	0.513703	0.348392	0.721900	0.241635	0.236478	0.628670
± 2 S.E.	0.000068	0.000016	0.000017	0.000000	0.000033	0.000025	0.000066
			Epsilon143=	20.78	using (143/144)chur=	0.512638	
			±	0.32	(Hamilton et al. 1983)		
linked from Sm sheet							
[Sm147]=	2.185833	nm/g			[Nd144]=	0.62207	nm/g
±	0.000412				±	0.00007	
[Sm]=	2.191532	ppm			[Nd]=	0.37727	ppm
±	0.000413				±	0.00004	
TOT ng Sm=	20.27715345				TOT ng Nd=	3.49066618	
		Sm147/Nd144=	3.513827				
		± 2 S.E.	0.000761				
		± 2RSE %	0.022%				

BOSTON COLLEGE PHOENIX

11-3-2017 version MJT

Full Sample Name: **M4 Gt D lch 1 ALQ1**
 Date of TIMS analysis: **6/9/22** Position #: **3**
 estimated Nd load (ng): **5.6**

Rspike Values Nd {SmNd 1.0 A spike, 6-12-08 calib}						
142/144	143/144	145/144	146/144	148/144	150/144	[Nd150]
0.830433	0.494001	0.436936	0.885201	0.740574	198.371260	0.049114
						nm/g

Wt Sample (g)= **0.0026562** g
 Wt Spike (g)= **0.12112** g

Mass Spectrometer Information:

Number of cycles measured:	195	
Number of cycles used:	180	
	start	average (from sheet)
Filament Current range: from	3.53	3.5325
		Amps
Beam intensity range: from	0.15119697	0.307467962
		Volts 144Nd.160
Temperature range: from	1513.333333	1548.166667
		° C

Final Ratio Data:

Interference Values (oxide corrected; informational only... not used in this sheet)

Ce140/Nd144 **0.015754773**
 Pr141/Nd144 **0.010321386**
 Sm149/Nd144 **8.92977E-05**

for Ratios & %ISE: use grand mean oxygen corr, interference corr, exp normalized values

	142/144	143/144	145/144	146/144	148/144	150/144
Ratios	1.1417149	0.51340379	0.34856595	0.7219	0.24287206	0.89716297
%StdErr	0.00102891	0.000640817	0.001098931	0	0.00288595	0.001987351
for comparison only	142/144	143/144	145/144	146/144	148/144	150/144
DePaolo 88, p.14, ln. B':	1.141854	na	0.348416	0.721882	0.241572	na

FINAL DATA TO REPORT:

		146/144 set to 0.7219					
	142/144	143/144	145/144	146/144	148/144	150/144	150t/144s
Ratios	1.141882	0.513272	0.348402	0.721900	0.241568	0.236478	1.502148
± 2 S.E.	0.000023	0.000007	0.000008	0.000000	0.000014	0.000009	0.000060
			Epsilon143=	12.37	using (143/144)chur=	0.512638	
			±	0.13	(Hamilton et al. 1983)		
linked from Sm sheet	[Sm147]= 2.599222	nm/g			[Nd144]= 3.36412	nm/g	
	± 0.000302				±	0.00019	
	[Sm]= 2.605999	ppm			[Nd]= 2.04026	ppm	
	± 0.000302				±	0.00011	
TOT ng Sm=	6.922053726				TOT ng Nd=	5.419325706	
		Sm147/Nd144=	0.772630				
		± 2 S.E.	0.000100				
		± 2RSE %	0%				

Full Sample Name: **M4 Gt D lch2 ALQ1**
 Date of TIMS analysis: **6/10/22** Position #: **5**
 estimated Nd load (ng): **<enter!>**

Rspike Values Nd {SmNd 1.0 A spike, 6-12-08 calib}						
142/144	143/144	145/144	146/144	148/144	150/144	[Nd150]
0.830433	0.494001	0.436936	0.885201	0.740574	198.371260	0.049114
						nm/g

Wt Sample (g)= **0.00288716** g
 Wt Spike (g)= **0.11866** g

Mass Spectrometer Information:

Number of cycles measured:	147	
Number of cycles used:	137	
		average (from sheet)
Filament Current range: from	3.36	3.41
Beam intensity range: from	0.084358739	0.131174321
Temperature range: from	1527	1556
		Amps
		Volts 144Nd.160
		° C

Final Ratio Data:

Interference Values (oxide corrected; informational only... not used in this sheet)

Ce140/Nd144	0.056057493
Pr141/Nd144	0.036816108
Sm149/Nd144	0.000822244

for Ratios & %1SE: use grand mean oxygen corr, interference corr, exp normalized values

	142/144	143/144	145/144	146/144	148/144	150/144
Ratios	1.1414774	0.51387974	0.34880252	0.7219	0.24472525	1.8322174
%StdErr	0.002301516	0.002422987	0.001571656	0	0.00436613	0.008827484
for comparison only	142/144	143/144	145/144	146/144	148/144	150/144
DePaolo 88, p.14, ln. B:	1.141854	na	0.348416	0.721882	0.241572	na

FINAL DATA TO REPORT:							
146/144 set to 0.7219							
	142/144	143/144	145/144	146/144	148/144	150/144	150t/144s
Ratios	1.141885	0.513564	0.348406	0.721900	0.241573	0.236478	0.616998
± 2 S.E.	0.000053	0.000025	0.000011	0.000000	0.000021	0.000042	0.000109
Epsilon143=				18.06	using (143/144)chur=		0.512638
				± 0.48	(Hamilton et al. 1983)		
linked from Sm sheet							
[Sm147]=	2.257315	nm/g	[Nd144]=			1.24544	nm/g
	± 0.000486					±	0.00022
[Sm]=	2.263201	ppm	[Nd]=			0.75532	ppm
	± 0.000487					±	0.00013
TOT ng Sm=	6.534223061		TOT ng Nd=			2.18074376	
	Sm147/Nd144=		1.812471				
	± 2 S.E.		0.000505				
	± 2RSE %		0.028%				

Multi-Collector Results : Nd (w/off line Interference, Oxygen Spike Subtraction)

Full Sample Name: **M4 Gt D lch 3 ALQ 1**
 Date of TIMS analysis: **6/13/22** Position #: **17**
 estimated Nd load (ng): **<enter!>**

Rspike Values Nd {SmNd 1.0 A spike, 6-12-08 calib}						
142/144	143/144	145/144	146/144	148/144	150/144	[Nd150]
0.830433	0.494001	0.436936	0.885201	0.740574	198.371260	0.049114
						nm/g

Wt Sample (g)= **0.00587607** g
 Wt Spike (g)= **0.13533** g

Mass Spectrometer Information:

Number of cycles measured:	74	
Number of cycles used:	68	
	start	average (from sheet)
Filament Current range: from	3.16	3.16
Beam intensity range: from	0.144414303	0.234453538
Temperature range: from	1520	1563
		Amps
		Volts 144Nd.160
		° C

Final Ratio Data:

Interference Values (oxide corrected; informational only... not used in this sheet)

Ce140/Nd144	0.037469898
Pr141/Nd144	0.02068986
Sm149/Nd144	0.000768325

for Ratios & %1SE: use grand mean oxygen corr, interference corr, exp normalized values

	142/144	143/144	145/144	146/144	148/144	150/144
Ratios	1.1411752	0.51475139	0.34900795	0.7219	0.24636593	2.6607598
%StdErr	0.002014142	0.001216596	0.00135209	0	0.003209899	0.004240565
for comparison only	142/144	143/144	145/144	146/144	148/144	150/144
DePaolo 88, p.14, ln. B:	1.141854	na	0.348416	0.721882	0.241572	na

FINAL DATA TO REPORT:							
146/144 set to 0.7219							
	142/144	143/144	145/144	146/144	148/144	150/144	150t/144s
Ratios	1.141799	0.514278	0.348404	0.721900	0.241574	0.236478	0.403246
± 2 S.E.	0.000046	0.000013	0.000009	0.000000	0.000016	0.000020	0.000034
				Epsilon143=	31.99	using (143/144)chur= 0.512638	
				±	0.24	(Hamilton et al. 1983)	
<i>linked from Sm sheet</i>							
[Sm147]=	2.046754	nm/g			[Nd144]=	0.45612	nm/g
	± 0.000458					± 0.00004	
[Sm]=	2.052091	ppm			[Nd]=	0.27663	ppm
	± 0.000459					± 0.00002	
TOT ng Sm=	12.05822798			TOT ng Nd=	1.625474897		
		Sm147/Nd144=	4.487299				
		± 2 S.E.	0.001075				
		± 2RSE %	0%				

Multi-Collector Results : Nd (w/off line Interference, Oxygen Spike Subtraction)

Full Sample Name: **M4 Gt Pwd 3 lch 1 ALQ1**
 Date of TIMS analysis: **6/10/22** Position #: **4**
 estimated Nd load (ng): **4.5**

Rspike Values Nd [SmNd 1.0 A spike, 6-12-08 calib]						
142/144	143/144	145/144	146/144	148/144	150/144	[Nd150]
0.830433	0.494001	0.436936	0.885201	0.740574	198.371260	0.049114 nm/g

Wt Sample (g)= **0.0023828** g
 Wt Spike (g)= **0.10154** g

Mass Spectrometer Information:

Number of cycles measured:	240	
Number of cycles used:	218	
	start	average (from sheet)
Filament Current range: from	3.56	3.59
Beam intensity range: from	0.051961217	0.141103374
Temperature range: from	1527	1565

Amps
Volts 144Nd.160
°C

Final Ratio Data:

Interference Values (oxide corrected; informational only... not used in this sheet)

Ce140/Nd144 **0.022875994**
 Pr141/Nd144 **0.011556688**
 Sm149/Nd144 **0.000238986**

for Ratios & %1SE: use grand mean oxygen corr, interference corr, exp normalized values

	142/144	143/144	145/144	146/144	148/144	150/144
Ratios	1.1417428	0.51340566	0.3485645	0.7219	0.24284086	0.89076006
%StdErr	0.001543315	0.001112561	0.001682184	0	0.003907852	0.004141701
for comparison only	142/144	143/144	145/144	146/144	148/144	150/144
DePaolo 88, p.14, ln. B:	1.141854	na	0.348416	0.721882	0.241572	na

FINAL DATA TO REPORT:							
146/144 set to 0.7219							
	142/144	143/144	145/144	146/144	148/144	150/144	150t/144s
Ratios	1.141908	0.513276	0.348402	0.721900	0.241550	0.236478	1.516931
± 2 S.E.	0.000035	0.000011	0.000012	0.000000	0.000019	0.000020	0.000126
Epsilon143=				12.44	using (143/144)chur=		0.512638
				± 0.22	(Hamilton et al. 1983)		
<i>linked from Sm sheet</i>							
[Sm147]=	2.404339	nm/g	[Nd144]=			3.17482	nm/g
	± 0.000376					± 0.00029	
[Sm]=	2.410608	ppm	[Nd]=			1.92545	ppm
	± 0.000377					± 0.00018	
TOT ng Sm=	5.743997382		TOT ng Nd=		4.587959372		
	Sm147/Nd144=		0.757315				
	± 2 S.E.		0.000137				
	± 2RSE %		0%				

Multi-Collector Results : Nd (w/off line Interference, Oxygen Spike Subtraction)

Full Sample Name: **M4 Gt Pwd 3 lch 2 ALQ 1**
 Date of TIMS analysis: **6/13/22** Position #: **6**
 estimated Nd load (ng): **5.6**

Rspike Values Nd {SmNd 1.0 A spike, 6-12-08 calib}						
142/144	143/144	145/144	146/144	148/144	150/144	[Nd150]
0.830433	0.494001	0.436936	0.885201	0.740574	198.371260	0.049114 nm/g

Wt Sample (g)= **0.003272** g
 Wt Spike (g)= **0.12487** g

Mass Spectrometer Information:

Number of cycles measured:	105	
Number of cycles used:	94	
		average (from sheet)
Filament Current range: from	3.41	3.42 Amps
Beam intensity range: from	0.116218127	0.294740004 Volts 144Nd.16O
Temperature range: from	1533	1584 °C

Final Ratio Data:

Interference Values (oxide corrected; informational only... not used in this sheet)

Ce140/Nd144 **0.028948877**
 Pr141/Nd144 **0.014005244**
 Sm149/Nd144 **0.000607791**

for Ratios & %1SE: use grand mean oxygen corr, interference corr, exp normalized values

	142/144	143/144	145/144	146/144	148/144	150/144
Ratios	1.1416501	0.51355341	0.34864412	0.7219	0.24345332	1.1842065
%StdErr	0.002003738	0.000985185	0.001111356	0	0.003289086	0.004816673
for comparison only	142/144	143/144	145/144	146/144	148/144	150/144
DePaolo 88, p.14, ln. B:	1.141854	na	0.348416	0.721882	0.241572	na

FINAL DATA TO REPORT:								146/144 set to 0.7219	
	142/144	143/144	145/144	146/144	148/144	150/144	150t/144s		
Ratios	1.141891	0.513365	0.348409	0.721900	0.241583	0.236478	1.044633		
± 2 S.E.	0.000046	0.000010	0.000008	0.000000	0.000016	0.000023	0.000101		
			Epsilon143=	14.18	using (143/144)chur=	0.512638			
			±	0.20	(Hamilton et al. 1983)				
linked from Sm sheet									
[Sm147]=	2.107205	nm/g			[Nd144]=	1.95800	nm/g		
	± 0.000223					±	0.00020		
[Sm]=	2.112699	ppm			[Nd]=	1.18748	ppm		
	± 0.000223					±	0.00012		
TOT ng Sm=	6.9127506				TOT ng Nd=	3.885425652			
		Sm147/Nd144=	1.076203						
		± 2 S.E.	0.000157						
		± 2RSE %	0%						

Multi-Collector Results : Nd (w/off line Interference, Oxygen Spike Subtraction)

Full Sample Name: **M4 Gt Pwd 3 residue**
 Date of TIMS analysis: **6/13/22** Position #: **18**
 estimated Nd load (ng): **3.5**

Rspike Values Nd {SmNd 1.0 A spike, 6-12-08 calib}						
142/144	143/144	145/144	146/144	148/144	150/144	[Nd150]
0.830433	0.494001	0.436936	0.885201	0.740574	198.371260	0.049114 nm/g

Wt Sample (g)= **0.00918** g
 Wt Spike (g)= **0.18449** g

Mass Spectrometer Information:

Number of cycles measured:	240	
Number of cycles used:	223	
		average (from sheet)
Filament Current range: from	3.12	3.18 Amps
Beam intensity range: from	0.058343218	0.073442325 Volts 144Nd.160
Temperature range: from	1520	1563 °C

Final Ratio Data:

Interference Values (oxide corrected; informational only... not used in this sheet)

Ce140/Nd144	0.04923108
Pr141/Nd144	0.020284861
Sm149/Nd144	0.001065544

for Ratios & %1SE: use grand mean oxygen corr, interference corr, exp normalized values

	142/144	143/144	145/144	146/144	148/144	150/144
Ratios	1.1415771	0.51433567	0.34875028	0.7219	0.24451015	1.709545
%StdErr	0.002160063	0.0022121	0.002047406	0	0.005925622	0.007165543
for comparison only	142/144	143/144	145/144	146/144	148/144	150/144
DePaolo 88, p.14, ln. B:	1.141854	na	0.348416	0.721882	0.241572	na

FINAL DATA TO REPORT:							
146/144 set to 0.7219							
	142/144	143/144	145/144	146/144	148/144	150/144	150t/144s
Ratios	1.141953	0.514047	0.348384	0.721900	0.241601	0.236478	0.669081
± 2 S.E.	0.000049	0.000023	0.000014	0.000000	0.000029	0.000034	0.000096
Epsilon143=				27.49	using (143/144)chur=		0.512638
				± 0.44	(Hamilton et al. 1983)		
<i>linked from Sm sheet</i>							
[Sm147]=	2.143492	nm/g	[Nd144]=		0.66041	nm/g	
	± 0.000392				± 0.00010		
[Sm]=	2.149081	ppm	[Nd]=		0.40052	ppm	
	± 0.000393				± 0.00006		
TOT ng Sm=	19.72856154		TOT ng Nd=		3.676786973		
	Sm147/Nd144=		3.245703				
	± 2 S.E.		0.000757				
	± 2RSE %		0%				

Multi-Collector Results : Nd (w/off line Interference, Oxygen Spike Subtraction)